Published in final edited form as:

Neuron. 2022 September 21; 110(18): 2929–2948.e8. doi:10.1016/j.neuron.2022.06.021.

Molecular signatures underlying neurofibrillary tangle susceptibility in Alzheimer's disease

Marcos Otero-Garcia[1], **Sameehan U. Mahajani**[1], **Debia Wakhloo**[1], **Weijing Tang**[1], **Yue-Qiang Xue**[1], **Samuel Morabito**[4,5], **Jie Pan**[1], **Jane Oberhauser**[1], **Angela E. Madira**[1], **Tamara Shakouri**[2], **Yongning Deng**[2,3], **Thomas Allison**[6], **Zihuai He**[7], **William E. Lowry**[8], **Riki Kawaguchi**[9], **Vivek Swarup**[5,10], **Inma Cobos**[1,11,*]

[1]Department of Pathology, Stanford University School of Medicine, Stanford, CA 94305, USA

[2]Department of Pathology, University of California, Los Angeles, CA 90095, USA

[3]Department of Neurology, First Affiliated Hospital of Xi'an Jiaotong University, Xi'an, Shaanxi, China

[4]Mathematical, Computational and Systems Biology Program, University of California, Irvine, CA 92697, USA

[5]Institute for Memory Impairments and Neurological Disorders, University of California, Irvine, CA 92697, USA

[6]Department of Biological Chemistry, University of California, Los Angeles, CA 90095, USA

[7]Department Neurology and Neurological Sciences, and Quantitative Sciences Unit, Department of Medicine, Stanford University, Stanford, CA 94305, USA

[8]Department of Molecular Cell and Developmental Biology, Broad Center for Regenerative Medicine, and Molecular Biology Institute, University of California, Los Angeles, CA 90095, USA

[9]Department of Psychiatry, and Semel Institute for Neuroscience and Human Behavior, University of California, Los Angeles, CA 90095, USA

[10]Department of Neurobiology and Behavior, University of California, Irvine, CA 92697, USA

[11]Lead contact

SUMMARY

---

[*]Correspondence: icobos@stanford.edu.

AUTHOR CONTRIBUTIONS

Conceptualization, I.C. and M.O.G.; Methodology, M.O.G. and I.C.; Investigation, M.O.G., I.C., Y.X. and Y.D.; Validation, J.P., J.O., A.M., T.S. and D.W; Formal Analysis, M.O.G., I.C., S.U.M., W.T., S.M., Z.H., R.K., T.A. and D.W.; Writing – Original Draft: I.C., M.O.G., J.P. and S.U.M.; Writing – Review & Editing: I.C., J.O.; Funding Acquisition, I.C., V.S. and W.E.L.; Supervision, I.C., V.S. and W.E.L.

DECLARATION OF INTERESTS

The authors declare no competing interests.

Tau aggregation in neurofibrillary tangles (NFTs) is closely associated with neurodegeneration and cognitive decline in Alzheimer's disease (AD). However, the molecular signatures that distinguish between aggregation-prone and aggregation-resistant cell states are unknown. We developed methods for the high-throughput isolation and transcriptome profiling of single somas with NFTs from human AD brain, quantified the susceptibility of 20 neocortical subtypes for NFT formation and death, and identified both shared and cell-type-specific signatures. NFT-bearing neurons shared a marked upregulation of synaptic transmission-related genes, including a core set of 63 genes enriched for synaptic vesicle cycling. Oxidative phosphorylation and mitochondrial dysfunction were highly cell-type dependent. Apoptosis was only modestly enriched, and the susceptibilities of NFT-bearing and NFT-free neurons for death were highly similar. Our analysis suggests that NFTs represent cell-type-specific responses to stress and synaptic dysfunction. We provide a resource for biomarker discovery and the investigation of tau-dependent and tau-independent mechanisms of neurodegeneration.

eTOC Blurb

Using a new method for profiling single, tangle-bearing neurons from postmortem brain tissue, Otero-Garcia et al quantify the susceptibility of 20 neocortical subtypes to tangle formation, define signatures of NFT susceptibility, and distinguish molecular changes specifically associated with NFTs from those broadly identified in Alzheimer's disease.

INTRODUCTION

AD pathology is defined by amyloid-β (Aβ) plaques and intracellular hyperphosphorylated tau aggregates in neurofibrillary tangles (NFTs) (Braak and Braak, 1991; Hyman et al., 2012; Serrano-Pozo et al., 2011). In neocortex, plaque buildup begins years before the onset of cognitive deficits, while NFTs appear later and progress in parallel with cognitive decline (Braak and Del Tredici, 2015; Nelson et al., 2012). Due to the association of tau pathology with regional brain atrophy and neuronal and synaptic loss, NFTs have largely been viewed as pathogenic (Ballatore et al., 2007; Jack et al., 2010; Nelson et al., 2012; Terry et al., 1991). Hyperphosphorylated tau appears to contribute to neurodegeneration by disrupting axonal transport and synaptic function, affecting the cellular stress response, and promoting neuroinflammation (Busche et al., 2019; Malpetti et al., 2020; Sherman et al., 2016; Zhou et al., 2017). Pathological tau may also contribute to disease progression by spreading toxic species through synapses (Franzmeier et al., 2019; Gibbons et al., 2019; Vogel et al., 2020). However, whether tau aggregation is toxic or protective—a main driver of neurodegeneration or part of a homeostatic response to cellular injury—remains unclear (Ittner et al., 2016; Kuchibhotla et al., 2014; Lewis and Dickson, 2016; Wang and Mandelkow, 2016).

Previous studies have identified brain regions and neuronal subtypes susceptible to tau pathology in AD, including hippocampal CA1, entorhinal cortex layer 2, and neocortical layer 2-3 and 5 pyramidal neurons (Bussière et al., 2003a; Gómez-Isla et al., 1996; Hof et al., 1990). Immunohistochemistry (IHC) and *in situ* hybridization (ISH) studies have demonstrated the susceptibility of excitatory projection vs. GABAergic inhibitory neurons (Fu et al., 2019; Hof et al., 1991; Hof et al., 1993; Saiz-Sanchez et al., 2015). Bulk

RNA-seq and network-based analysis suggested vulnerability of certain pathways to tau, including microtubule-related pathways (Roussarie et al., 2020), the heat-shock response, and autophagy (Fu et al., 2019). Despite these advances, the heterogeneity of cellular and transcriptional responses associated with tau pathology in human AD has not been resolved.

Transcriptome profiling of single cells or nuclei (snRNA-seq) can resolve cellular heterogeneity and predict pathological cellular states (Darmanis et al., 2015; Habib et al., 2017; Hodge et al., 2019; Lake et al., 2016). Studies comparing nuclear gene expression to whole cells have shown a high degree of concordance (Bakken et al., 2018; Grindberg et al., 2013; Lake et al., 2017). snRNA-seq has been successfully applied to frozen human AD brains, revealing shared and cell-type-specific gene expression changes, sex-biased transcriptional responses, and potential drivers of disease progression (Del-Aguila et al., 2019; Grubman et al., 2019; Leng et al., 2021; Mathys et al., 2019). However, nuclear profiling cannot distinguish between cells with and without cytoplasmic aggregates, like NFTs. Laser-capture microdissection allows the profiling of individual NFT-bearing cells (Dunckley et al., 2006; Tagliafierro et al., 2016), but is low-throughput and may present sampling bias. Profiling whole cells from fresh brain tissue is feasible (Darmanis et al., 2015), but presents low yield biased toward glial cell recovery. The difficulty of obtaining fresh tissue from unique clinical samples and diseases managed non-surgically, such as neurodegenerative dementias, represent another limitation.

We developed a fluorescence-activated cell sorting (FACS) based method for the high-throughput isolation of somas with NFTs and profiled 63,110 somas with or without NFTs from the prefrontal cortex of Braak VI AD donors, and 57,534 somas from age-matched controls. This method allowed us to quantify the susceptibility of 20 cortical neuronal subtypes for NFT formation and death, to characterize molecular signatures of NFT susceptibility within and across subtypes, and to distinguish molecular changes associated with NFTs from those commonly altered in AD. By comparing NFT-bearing and neighboring NFT-free somas, we obtained unbiased, precise identification of the neuronal subtypes exhibiting aggregates. NFT-bearing neurons shared a marked upregulation of genes related to synaptic transmission, particularly the synaptic vesicle cycle. We provide a ranked list of 227 synaptic genes associated with NFTs, including a core set of 63 genes shared across neuronal subtypes. Genes encoding neurodegeneration biomarkers *NEFL, SNAP25*, and *SYT1* sat within the top 25, highlighting the value of our datasets for discovery. By comparing the transcriptomes of non-AD and AD (NFT-bearing and NFT-free) somas, we distinguished between susceptibility for NFT formation and cell death. Our analysis reveals a modest association between NFTs and death and suggests that NFT-bearing neurons may represent a cellular response to stress and synaptic dysfunction.

RESULTS

Isolation and transcriptome profiling of single somas with NFTs

Since the standard methods for profiling nuclei from human brain (Habib et al., 2017; Krishnaswami et al., 2016; Lake et al., 2016) cannot distinguish between cells with and without cytoplasmic aggregates, we developed procedures for the high-throughput isolation and profiling of NFT-bearing somas (Figures 1A-1D, 1F). First, we optimized the isolation of cells with well-preserved somas. We microdissected gray matter from prefrontal cortex (BA9), brainstem, and basal ganglia, and applied gentle mechanical dissociation without detergents or enzymatic digestion. Using a tissue grinder with a wider clearance between the pestle and tube than those typically used for nuclei facilitated the dissociation of larger somas (Figure 1A). We then performed sucrose-iodixanol gradient centrifugation with adjusted parameters for density barrier composition, centrifugal force, and time to eliminate debris and obtain an enriched soma fraction. Microscopic examination showed neurons with well-preserved somas, including pyramidal cell bodies with proximal dendrites (Figure 1B).

To compare single-soma and single-nucleus profiling, we used pan-neuronal markers MAP2 (cytoplasmic) and NeuN (nuclear) to sort single somas or nuclei by FACS and analyze the transcriptomes of 74,283 cells from the BA9 of four healthy donors (Figure S1A). MAP2$^+$ cells had modest increases in the median number of genes per cell (2,210 vs. 2,086 for NeuN) and higher mitochondrial gene content (1.49% vs. 0.18% for NeuN) (Figure S1B), indicating efficient profiling of nuclear transcripts using both methods and limited cytoplasmic transcripts from MAP2$^+$ cells. This outcome is expected in frozen tissues whose cell membranes have been disrupted and most cytoplasmic transcripts lost. To assess whether single-soma isolation was biased toward the recovery of specific neuronal subtypes, we compared the relative percentages of 20 subtypes derived from soma or nuclear homogenates. Both methods yielded highly similar cell compositions, except for an increased recovery of two rarer excitatory subtypes by soma isolation (Ex3: 3.02 ± 0.30% vs. 1.36 ± 0.13% for nuclei; Ex5: 2.83 ± 0.16% vs. 2.05 ± 0.11% for nuclei; Figure S1F). Thus, the ability to discriminate between neuronal subtypes remained highly similar using both methods (Figures S1C-G).

Next, we applied our method to NFT-bearing somas from AD donors. Immunostaining and FACS using MAP2 and the AT8 antibody, which detects hyperphosphorylated tau aggregates, allowed us to isolate single NFT-bearing somas (MAP2$^+$/AT8$^+$; referred to as AT8$^+$) and neighboring NFT-free somas (MAP2$^+$/AT8$^-$; referred to as AT8$^-$) from the same homogenate. As in IHC and immunoblotting, AT8 labeled pretangles and mature tangles in fresh somas (Moloney et al., 2021; Wesseling et al., 2020) (Figure 1D). It overlapped with populations sorted by FACS using T22, an antibody against oligomeric tau enriched in pretangles, and PHF1, which is enriched in mature and ghost tangles (~ 82% and 89% overlap, respectively; Figure S2). Our method could also isolate glial cells with tau aggregates, as shown by FACS of the MAP2$^-$/AT8$^+$ population from donors with progressive supranuclear palsy (PSP), a primary tauopathy with both neuronal and glial aggregates (Figure 1E).

Census of neuronal subtypes exhibiting NFTs in the prefrontal cortex of human AD brain

To determine the cellular specificity of NFTs, we profiled AT8$^+$ and AT8$^-$ somas from the BA9 of eight Braak VI AD donors (Table S1). NFTs were present in 6.3 ± 1.15% of all neurons in histological sections from the same tissue blocks used for transcriptomics (Figure 2A). We analyzed 24,660 AT8$^+$ and 38,465 AT8$^-$ single transcriptomes. The median numbers of genes and UMIs per soma were ~ 18% higher in AT8$^+$ (1,481 and 2,440, respectively) than in AT8$^-$ somas (1,248 and 2,062; paired t-test; $p = 0.01$ and $p = 0.02$, respectively; Figures 2B and 2C). The increase in UMIs and genes in AT8$^+$ somas may have resulted from differences in cell composition (i.e., higher transcript abundance in larger cells) and/or transcriptional upregulation.

Unsupervised clustering of the NFT-free (AT8$^-$) dataset identified a cell composition concordant with published datasets from control and AD nuclei (Hodge et al., 2019; Mathys et al., 2019) (Figures 2B and S1D). Using conservative parameters, we annotated 17 clusters including 11 expressing the pan-excitatory marker *SLC17A7* and 6 expressing the pan-inhibitory marker *GAD1* ("Ex" and "In" clusters; Figure S1D). Excitatory subtypes included layers 2–4 *CUX2* (superficial *LAMP5/SERPINE* [Ex1] and deeper *COL5A2* cells [Ex2]); layers 4/5 *RORB* (*RORB/PLCH1/MME/GAL, RORB/GABGR1, RORB/RPRM, RORB/PCP4* [Ex3, Ex4/5, Ex6, Ex7]); layer 5b *PCP4/ROBO3* [Ex8]; layers 5/6 *NFIA/THEMIS* [Ex10]; layer 6 *THEMIS/NR4A2/NTNG2* [Ex11] and *FEZF2/SYT6* [Ex12]; and deeper layer 6b *FEZF2/SEMA3D/CTGF* [Ex13] cells. Inhibitory subtypes included two major classes with developmental origins in the medial (*LHX6*) and caudal (*ADARB2*) ganglionic eminences (MGE, CGE). *LHX6* cells consisted of *PVALB* and *SST* subtypes. A distinct *PVALB* cluster characterized by high expression of *GAD1*, low expression of *GAD2*, and expression of *SCUBE3* defined putative chandelier cells (Hodge et al., 2019). *ADARB2* cells included *LAMP5/KIT* cells (split into two clusters by expression of *CXCL14*) and a highly heterogeneous *VIP/CALB2* cluster. The proportion of inhibitory cells was 26.6%. Thus, all major neuronal subtypes were identified in BA9 from Braak VI AD patients, despite neuronal loss in this region throughout disease progression (Bussière et al., 2003b; Frisoni et al., 2010; Serrano-Pozo et al., 2011).

Unsupervised clustering of the NFT-bearing (AT8$^+$) dataset using the same pipeline showed clusters corresponding to cell types and technical covariates. Multiple canonical correlation analysis (multiCCA) (Butler et al., 2018) enhanced cell identity-based clustering and removed clusters originating from individual samples. We annotated 8 excitatory and 2 inhibitory clusters (94% and 3.2% of total cells, respectively) (Figure 2C). The excitatory clusters were less distinct, likely resulting from cell state variation associated with tau pathology. Some excitatory subtypes were not identified, likely due to the small number of cells in those subtypes.

To obtain a census of neuronal subtypes exhibiting NFTs, we integrated the AT8$^+$ and AT8$^-$ datasets using multiCCA (Figures 2D-F). We annotated the same 17 neuronal subtypes as in the AT8$^-$ dataset (Figures 2E and 2F). Clustering was not driven by particular samples, as all eight donors contributed cells evenly (Figure 2G). The results were consistent across clustering algorithms and robust to clustering parameter variation (Figure S3). We counted the number of AT8$^+$ and AT8$^-$ somas within each cluster (Figures 2H and 2I; Table S2) and normalized the cell counts to NFT density by tissue section (Figure 2A). The proportion of AT8$^+$ neurons ranged from 1.0–11.7% for excitatory and 0.5–6.8% for inhibitory subtypes (Figure 2I). The subtypes with the highest NFT proportion were layers 2–4 *CUX2* (Ex1 and Ex2; 11.7% and 10.5%, respectively) and layer 5 *RORB/PCP4* (Ex7; 10.6%). Notably, layer 5 was heterogenous and contained highly susceptible (Ex7) and less susceptible (*RORB/GABGR1* [Ex4/5] and *RORB/RPRM* [Ex6]; 3.6% and 5.2%, respectively) subtypes (Figures 2I, 3B, and 3D). Layer 6 was largely spared, although a deep layer 6b subpopulation showed intermediate proportions of NFTs (Ex11; 5.6%). Most inhibitory neurons were spared (overall 1.9%), except for chandelier cells (In2; 6.8%) (Figure 2I).

To validate markers for susceptible neuronal subtypes, we used histological sections from the same tissue blocks (Figure 3). Combined IHC for AT8 and ISH for *SLC17A7* and *GAD1* showed proportions of NFTs in excitatory (11.59 ± 3.7%) and inhibitory neurons (0.95 ± 0.41%) similar to those in our transcriptome analysis (Figures 3A and 3F). Layer 2-3 neurons expressing *CUX2* and either *LAMP5* (Ex1) or *COL5A2* (Ex2), showed high NFT proportions (10.64 ± 4.2%; Figures 3C and 3F). Layer 5 neurons expressing *PCP4*, including *RORB/PCP4* (Ex7) and layer 5b *PCP4/ROBO3* (Ex8) neurons, were susceptible (12.24 ± 4.2% and 5.70 ± 2.53%, respectively; Figures 3D and 3F). The layer 6 *NR4A2/NTNG2* (Ex11) subtype was largely spared (0.5 ± 0.3%; Figures 3E and 3F). NFT proportions obtained by histology were consistent with those in our transcriptome analysis (Figures 2I and 3F), except for the *PCP4/ROBO3* cluster (9.6% vs. 5.7%), likely due to the low number of *ROBO3* transcripts detected by RNAscope ISH. Thus, various subpopulations of excitatory and inhibitory neurons demonstrate markedly different susceptibilities to NFT formation. This specificity can be resolved via single-soma transcriptomics.

Signatures of NFT susceptibility within and across excitatory neuronal subtypes

To define shared and cell-type-specific molecular signatures of NFT susceptibility, we performed a two-step differential gene expression (DGE) analysis, first between NFT-bearing and NFT-free neurons within each subtype, and then comparing differentially expressed (DE) genes across subtypes. Using the MAST (model-based analysis of single-cell transcriptomics) generalized linear model (Finak et al., 2015) for DGE analysis within each subtype, we identified 692–978 DE genes in clusters with high cell numbers and NFT proportions (Ex1, Ex2, Ex3, Ex7, Ex10) and 55–186 DE genes in the smaller clusters (Figures 4A and 4B; Table S2) (MAST test; adjusted p-value < 0.05; log-fold change >0.1; detection in ≥ 20% of cells). Most DE genes were upregulated in NFT-bearing neurons (~66–84% upregulated in Ex1, Ex2, Ex7, Ex10), except in cluster Ex3 (~39% upregulated). This widespread transcriptional upregulation is consistent with previous work showing an association between hyperphosphorylated tau and chromatin remodeling (Frost et al., 2014; Klein et al., 2019). Overall, NFT-associated transcriptomic changes were robust to the subsampling of a subset of donors, as assessed by the rank-rank hypergeometric overlap (RRHO) test (Figure S4).

We then performed hierarchical clustering of DE genes across neuronal subtypes to identify cell-type-specific and shared changes (Figure 4C). We focused on five excitatory clusters with the highest cell numbers and NFT proportions (Ex1, Ex2, Ex3, Ex7, Ex10) to avoid underestimating the extent of shared changes. While many gene expression changes were subtype-specific, this approach distinguished 124 DE genes (102 upregulated; 22 downregulated) altered across all five clusters and 163 genes upregulated in all clusters except Ex3 (Figure 4C). Upregulated genes with the highest fold changes included genes encoding synaptic proteins (i.e., *CALM1, ATP1B1, GRIN2B, CDK5R1, SYT4, CANX, RTN4*) and cytoskeletal proteins and microtubule dynamics regulators (i.e., *ACTG1, TUBB2A, PLPPR4, MAP1A, ENC1, STMN2*). Other commonly upregulated genes included the immediate early gene *JUN*, the integrated stress response transcription factor *ATF4*, the gene encoding the heat shock protein and chaperone Hsp90 (*HSP90AA1*), the gene encoding the lysosomal protein prosaposin (*PSAP*), and the iron homeostasis-associated genes *FTL* and *FTH1* (Figure 4C). Notably, *APP*, which encodes Aβ precursor protein, was upregulated in neurons with NFTs in most clusters but not in Ex3. Similar changes were observed for the prion protein-coding gene (*PRNP*; Figure 4D), whose product acts as a receptor for soluble Aβ oligomers (Laurén et al., 2009).

To investigate the gene-regulatory networks underlying shared and cell-type-specific responses associated with tau, we performed transcription factor (TF) binding site enrichment analysis and generated TF regulatory networks integrating neuronal-specific ENCODE ChIP-seq data and consensus coexpression networks in AD (Mostafavi et al., 2018). Among the TF networks shared across neuronal subtypes was *REST*, a key regulator of neuronal differentiation and excitability previously implicated in aging and AD (Lu et al., 2014; Zullo et al., 2019). Cluster Ex3 had a unique set of TF networks including *GABPA*, a TF involved in nuclear regulation of mitochondrial function (Figures 4E and S5; Table S3) (Yang et al., 2014). Together, our DGE and gene regulatory network analyses identified shared and cell-type-specific molecular signatures associated with tau pathology across neuronal subtypes.

Shared versus cell-type-specific pathways associated with tau pathology

To visualize shared and cell-type-specific pathways associated with NFTs, we used functional enrichment analysis (Reimand et al., 2019) (Figure 5A). First, we generated a ranked list of statistically significant gene ontology (GO) terms enriched in NFT-bearing neurons for each cell type using g:Profiler (Figure 5B). Then, we integrated results from five highly susceptible clusters (Ex1, Ex2, Ex3, Ex7, Ex10) into a single network using Cytoscape with EnrichmentMap. The resulting enrichment map illustrates the pathways enriched in NFT neurons that were cell-type-specific or shared across subtypes (Figure 5C) and delineates the gene set associated with each dysregulated pathway (Table S4). The shared pathways with the highest enrichment scores were related to synaptic transmission (Figure 5C; Table S4). Other commonly enriched pathways included calcium homeostasis, microtubule polymerization, axonal remodeling, dendritic spine remodeling, microtubule-based transport, and intracellular protein transport. In contrast, glucose metabolism and oxidative phosphorylation were cell-type dependent and particularly enriched in Ex3. Notably, neuronal cell death and apoptosis pathways were shared across cell types but represented only modestly, with both pro- and anti-apoptotic regulators represented. Genes in this category included *FAIM2* and *MIF* (downregulated), and *ATF4, BAD, BNIP3*, and *HIF1A* (upregulated). A smaller set of genes involved in mitochondrial membrane permeability transition was upregulated, including *BAD, BNIP3, HSPA1A*, and genes encoding 14-3-3 phospho-serine/phospho-threonine binding proteins (*YWHAE, YWHAH, YWHAG, YWHAZ*, and *YWHAB*) (Figure 5C; Table S4). Collectively, our analysis identified shared and cell-type-specific pathways associated with tau pathology and highlighted the enrichment of synaptic transmission pathways in neurons with NFTs across subtypes.

Dysregulation of synaptic transmission pathways in neurons with NFTs

To further characterize synaptic transmission pathways in NFT-bearing neurons, we used SynGO, a reference for synaptic gene annotations and ontologies (Koopmans et al., 2019). We identified 24 cellular component and 37 biological process terms significantly enriched (Table S5). By cellular location, the postsynaptic density membrane, presynaptic membrane, and presynaptic active zone were overrepresented. Top-level overrepresented terms included synapse organization, process in the presynapse and process in the postsynapse, whereas metabolism and transport were underrepresented (Figures 6A and S6). The highest enrichment scores corresponded with the synaptic vesicle cycle (Figures 6A and 6B). The central role of synaptic vesicle cycle dysregulation in AD pathogenesis has also been suggested by previous omics and cellular studies (Canchi et al., 2019; de Wilde et al., 2016; Zhou et al., 2017).

A total of 227 DE genes in NFT-bearing neurons mapped to SynGO annotated genes (Table S5). The vast majority were upregulated (~89–95% in Ex1, Ex2, Ex6, Ex7), except in Ex3 (~60% downregulated). 17 genes were dysregulated in all 5 clusters, and 46 were dysregulated in 4 of 5 clusters (MAST test; adjusted p-value < 0.05; log-fold change > 0.1; detection in $\geq 20\%$ of cells) (Figures 6C and S6). Of these 227 genes, 15 are AD risk factors (*GRIN2B, NRXN3, CTNND2, NRN1, NCS1, CDH13, PTK2B, BCL11A, SHANK2, NRGN, FARP1, VCP, CAMK4, SYNGAP1, SYNJ1*) (Kunkle et al., 2019). Notably, among the commonly upregulated were three genes for biomarkers of neurodegeneration and cognitive decline in AD: neurofilament light chain protein (*NEFL*), synaptosomal–associated protein 25 (*SNAP25*), and synaptotagmin-1 (*SYT1*) (Brinkmalm et al., 2014; Davidsson et al., 1996; Mattsson et al., 2017) (Figures 6B and S6; Table S5). Other upregulated genes related to the synaptic vesicle cycle included *STY4* and *STY11*, *SV2B*, and *BSN*. Several ion channel and membrane potential regulators were commonly upregulated in NFT neurons, including genes for NMDA glutamate receptor subunits (*GRIN2B*, *GRIN2A*), $\mathrm{GABA_A}$ receptor subunits (*GABRA1*, *GABRG2*), $\mathrm{Na^+/K^+}$–ATPase subunits (*ATP1A3*, *ATP2B2*), and voltage-gated sodium channel Nav1.6 (*SCN8A*). Other commonly upregulated genes included *NTRK2*, encoding neurotrophic receptor tyrosine kinase 2 (TrkB), and *NRXN3*. No genes were downregulated in all 5 clusters, and only 2 genes were downregulated in 4 of the 5: *RIMS2*, encoding a Rab3-interacting protein implicated in synaptic vesicle exocytosis, and *PNKD*, whose product interacts with RIM proteins (Kaeser et al., 2012; Shen et al., 2015) (Figures 6C and S6).

To histologically validate the upregulation of synaptic markers in NFT-bearing neurons, we quantified *SNAP25, GABRA1, GRIN2B*, and *SYT1* transcripts in $\mathrm{AT8^+}$ vs. $\mathrm{AT8^-}$ excitatory neurons from the BA9 of four Braak VI AD donors (Figures 6D and 6E). The integrated density of all four synaptic markers was significantly increased in $\mathrm{AT8^+}$/*SLC17A7*$^+$ compared to $\mathrm{AT8^-}$/*SLC17A7*$^+$ layer 2-3 neurons, consistent with the upregulation of these markers in Ex1 and Ex2 (Figure 6F). Thus, our analysis identified a set of commonly dysregulated synaptic genes in neurons with NFTs that included well-established AD biomarkers, highlighting the value of our datasets for discovery.

Uncoupling of NFT and neuronal death susceptibilities in the AD prefrontal cortex

To analyze transcriptional changes associated with NFTs in the context of AD, we profiled control tissue with no AD pathology (BA9; 8 cognitively normal, age-matched donors; 57,534 somas) (Table S1), and integrated the control, NFT-bearing and NFT-free AD datasets (referred to as non-AD, AD-AT8^{+} and AD-AT8^{-}). This approach allowed us to determine whether neuronal subtypes prone to forming NFTs are equally susceptible to death.

Integration of the non-AD, AD-AT8^{+} and AD-AT8^{-} datasets (119,326 somas after QC) identified the same neuronal clusters as in our AD dataset. Additionally, we identified small clusters of putative layer 5b subcortical projection neurons (Ex9; 534 somas) and *SST/NPY* interneurons (In4; 194 somas). Ex4/5 split into two distinct subclusters (Ex4, Ex5; Figures 7A and 7B).

The BA9 shows atrophy and neuronal loss at Braak stage VI (Bussière et al., 2003b). To determine susceptibility to death, we obtained the relative fractions of somas within each cluster (13 excitatory and 7 inhibitory) in non-AD vs. AD (Figures 7C and 7D). If NFTs were a primary driver of toxicity and death, the neuronal subtypes harboring them (i.e., overall excitatory; particularly Ex1, Ex2, Ex7) would be relatively reduced at Braak VI. In contrast with the marked differences in susceptibility to NFTs across neuronal subtypes, we found only minor differences in their susceptibility to death (Figure S7). Because there was a non-statistically significant trend toward a decrease in total excitatory somas relative to total neuronal somas in AD vs. non-AD (75.06 ± 3.2% vs. 80.13 ± 2.9%; Figure 7D), we analyzed the excitatory and inhibitory populations separately. We found no differences across excitatory subtypes and detected a small but statistically significant increase in the susceptibility of *SST* interneurons to cell death (In3 & In4; Figure 7D).

To address susceptibility to death in the BA9 in two independent AD snRNA-seq studies (Leng et al., 2021; Mathys et al., 2019), we re-analyzed all datasets using the MapQuery function in Seurat v4. This tool enables harmonization by using consistent annotations across datasets. We transferred the annotations from our reference dataset (64,792 nuclei & somas; 4 donors; Braak 0–II; Figure S1) to the query datasets: Mathys *et al.* (44,123 neurons; 48 donors; Braak 0–VI), Leng *et al.* (23,339 neurons; 7 donors; Braak 0, II & VI), and ours (119,326 neurons; 16 donors; Braak 0–II & VI; Figure 7) and projected the query datasets onto the reference UMAP (Figures S8A and S8B). None of the query datasets showed statistically significant changes in neuronal cell composition as a function of Braak stage, except for a decrease in In3/4 (*SST*$^{+}$/*NPY*$^{+}$) and In6 (*LAMP5*$^{+}$) interneurons in high vs. low Braak stages in Mathys *et al.* (Figure S8C), supporting a lack of substantial cell-type-specific neuronal loss in the BA9 of AD patients.

Overall, our analysis showed that highly susceptible (layers 2–3 Ex1 & Ex2; layer 5 Ex7) and resistant (layers 4–5 Ex4–Ex6; layers 6 Ex11–Ex13) subtypes to NFT formation were neither more susceptible nor resistant to death. Although interneurons were generally resistant to forming NFTs, they were not spared from death. Chandelier interneurons were relatively susceptible to NFT formation, whereas SST interneurons were most susceptible to death. Our analysis suggests an uncoupling of NFT susceptibility from neuronal death, highlighting the existence of NFT-dependent and NFT-independent mechanisms contributing to neurodegeneration.

NFT-specific versus common AD associated transcriptome changes

To distinguish NFT-specific transcriptomic changes from those commonly altered in AD, we performed a three-way DGE analysis between non-AD, AD-AT8$^-$, and AD-AT8$^+$ datasets. First, we compared the number of DE genes between each pair: AD-AT8$^-$ vs. non-AD (referred to as Aβ-associated), AD-AT8$^+$ vs. non-AD (AD-associated), and AD-AT8$^+$ vs. AD-AT8$^-$ (NFT-associated) (Figure 8A and Table S6). Most Aβ-associated DE genes were downregulated (~79% to 53%; 276–1,203 DE genes in excitatory clusters excluding Ex9; MAST test with adjusted p-value < 0.05, log2 fold change > 0.2, detection in ≥ 20% of cells), consistent with previous studies showing a global transcriptional downregulation in human AD brain (Wan et al., 2020), and contrasting with the upregulation associated with NFTs (Figures 4A and 8B). Next, we obtained the numbers of up- and downregulated genes that were unique or shared between the three comparisons (Figure 8C and 8D; Ex1, Ex2, Ex3, Ex7, Ex10). We found a high degree of overlap between the three comparisons (55.7% to 69.5% of the DE genes), and relatively low numbers of DE genes that were NFT-specific (~4% to 7%; 54–146 DE genes) or NFT-independent (~8% to 16%; 145–280 DE genes) (Figures 8C and 8D). Most expression changes in the overlap group occurred in the same direction (~99%), and the log2 fold expression values were greater in association with NFTs (~8% to 23% for downregulated genes; ~9% to 58% for upregulated genes; AD-AT8$^+$ vs. non-AD compared to AD-AT8$^-$ vs. non-AD in Ex1, Ex2, Ex3, Ex7, Ex10) (Figure 8E and Table S6).

To visualize Aβ-associated, NFT-associated, and AD-associated pathways, we generated functional enrichment maps (Ex1, Ex2, Ex3, Ex7, Ex10; Figure 8F; Table S7). As expected, most enriched pathways were shared between all three groups. These included pathways related to the synapse (synaptic transmission, synapse assembly, calcium homeostasis, action potential regulation), the cytoskeleton (microtubule dynamics, axonal remodeling, microtubule-based transport), transport (intracellular protein transport, protein targeting to the membrane), and metabolism (oxidative phosphorylation, ATP synthesis). In contrast, pathways identified exclusively as NFT-associated or Aβ-associated were underrepresented. Notably, RNA splicing was underrepresented in the NFT-associated category. This pathway included the spliceosomal complex and nuclear speck genes *PDCD7, HNRNPU, FUS, SRSF10, SRRM2, RBM5*, and *SNU13* (Figure 8G and Table S7). Autophagy pathways were enriched in association with AD and with NFTs and included macroautophagy and regulation of autophagy by lysosomal pH (e.g., *BNIP3, IRS2, UBB, UBC, TSC1, TSC2, RHEB, CAMKK2, PIK3C3, MAPK1*). Correspondingly, we found an increase in SQSTM1/p62 protein expression in AT8$^+$ vs. AT8$^-$ FACS-sorted neuronal somas (Figure S9D), as previously reported in postmortem sections from AD patients (Piras et al., 2016). Neuronal death and neurodegeneration were also overrepresented in association with both AD and NFTs. This complex category included master regulators of neuronal survival, the stress response, and apoptosis: *UBB*, encoding ubiquitin (upregulated in AD); *BAD*, encoding Bcl-2 agonist of cell death protein (upregulated in AD and NFT-bearing); and *JUN* and *ATF4* (upregulated in NFT-bearing) (Figure 8G and Table S7). Notably, *ATF4*, the main effector of the integrated stress response, a common adaptive pathway for restoring cellular homeostasis (Pakos-Zebrucka et al., 2016), was highly upregulated in association with NFTs. We validated this finding using RNAscope ISH in histological sections (Figure S9A-C). Collectively, our analysis highlighted dysregulated genes and pathways enriched in an NFT-associated and NFT-independent manner in the AD brain.

DISCUSSION

Despite evidence linking tau pathology to histological and neuroimaging features of neurodegeneration in AD (Bejanin et al., 2017; Braak and Del Tredici, 2015; Franzmeier et al., 2019; Hanseeuw et al., 2019; Jack et al., 2018; Nelson et al., 2012; Schöll et al., 2016; Schwarz et al., 2016), the molecular signatures that distinguish between aggregation-prone and aggregation-resistant cell states remain undetermined. To address this, we developed procedures for the unbiased, high-throughput profiling of NFT-bearing neurons from fresh-frozen human brain.

A caveat of our method is the disruption of cell membranes by freeze-thawing which results in loss of most cytoplasmic transcripts. Our analysis comparing nuclear and soma FACS-sorted populations showed highly similar total gene and UMI content in both conditions; however 50–80% of transcripts are estimated to be cytoplasmic (Bakken et al., 2018; Grindberg et al., 2013). Variable cytoplasmic amounts may introduce bias in transcript quantification and/or cell recovery. To reduce this variability, we compared NFT-bearing and NFT-free somas processed in parallel from the same tissue sample. This strategy also reduced potential confounding effects from patients' genetics, sex, age, comorbidities, medication, and premortem agonal state. The loss of cytoplasmic transcripts did not undermine our method's ability to discriminate between closely related neuronal subtypes, as shown in previous snRNA-seq studies (Bakken et al., 2018; Lake et al., 2017). The relative abundance of each neuronal subtype was highly similar after sorting somas or nuclei, except for an increase in two relatively rare subtypes (Ex3, Ex5) in the soma preparations. This selection bias may be explained by technical differences in cell fractionation and/or immunostaining and should be considered particularly when analyzing mixed datasets from both nuclei and somas. Thus, we provide a method for profiling single cells with cytoplasmic protein aggregates. Our method can be applied to other tauopathies such as PSP, corticobasal degeneration, Pick's disease, primary age-related tauopathy (PART), and chronic traumatic encephalopathy to investigate shared and disease-specific mechanisms of tau-mediated neurodegeneration.

Previous studies have suggested morphological and molecular features that may underlie selective susceptibility of cortical neuronal subtypes to tau pathology. NFT formation has been associated with larger cell size, low expression of Ca^{2+}-binding proteins, sparse myelination, and dysregulation of autophagy and microtubule dynamics (Bussière et al., 2003a; Dunckley et al., 2006; Fu et al., 2018; Fu et al., 2019; Roussarie et al., 2020). Here, we demonstrate specificity of NFT formation in 20 neocortical neuronal subtypes. The subtypes with the highest proportions of NFTs included putative cortico-cortical projection neurons in layers 2–3 (Ex1, Ex2; *CUX2*$^{+}$) and intratelencephalic projection neurons in layer 5 (Ex7; *RORB/PCP4*$^{+}$) (Harris et al., 2019; Harris and Shepherd, 2015;

Zeng et al., 2012). Among cortico-thalamic neurons, a population of deep layer 6b neurons (Ex13; *FEZF2/CTGF*$^+$) that projects to anterior and mediodorsal (i.e., association) thalamic nuclei in rodents (Hoerder-Suabedissen et al., 2018; Zeng et al., 2012) was relatively vulnerable. Combined with previous studies showing the stereotypical distribution pattern of tau pathology and its spread through functionally connected brain regions (Braak and Braak, 1991; Braak and Del Tredici, 2018; Franzmeier et al., 2019; Rüb et al., 2016), these results support an association between tau pathology and neural connectivity. As previously suggested, vulnerable circuits may correspond to the default-mode network (Greicius et al., 2004; Raichle et al., 2001; Seeley et al., 2009).

Our DGE analysis comparing non-AD, AD-AT8$^-$, and AD-AT8$^+$ somas illustrated shared AD and NFT-associated pathways converging on the synapse, supporting the notion of AD as synaptopathy (de Calignon et al., 2010; de Wilde et al., 2016; Selkoe, 2002; Sheng et al., 2012; Spires-Jones and Hyman, 2014). Although the pathogenic cascade leading to synaptic failure in AD is incompletely understood, APP cleavage products, Aβ oligomers, and tau oligomers appear to play key roles (Busche et al., 2019; Moore et al., 2015; Pickett et al., 2019; Puzzo et al., 2017; Zott et al., 2019). We identified *APP* upregulation in NFT-bearing neurons across excitatory subtypes. APP/Aβ is upstream of tau pathology in AD, and duplication of *APP* causes early-onset AD (Hardy and Selkoe, 2002; Rovelet-Lecrux et al., 2006). Increased *APP* levels in NFT-bearing neurons may contribute to changes in gene expression via the APP intracellular domain (AICD), an APP cleavage product that translocates to the nucleus and acts as a transcriptional regulator (Cao and Südhof, 2001). NFT-bearing neurons may also modulate their response to extracellular, soluble Aβ through the expression of Aβ receptors. Putative cell surface receptors for Aβ upregulated in NFT-bearing neurons include *PRNP, GRIN2B, GRIN2A, ATP1A3, EPHA4*, and *PGRMC1* (Fu et al., 2014; Izzo et al., 2014; Laurén et al., 2009; Ohnishi et al., 2015; Shankar et al., 2007). Thus, our findings support a model in which *APP* upregulation and/or synaptic dysregulation in NFT-bearing neurons may contribute to neurodegeneration.

However, the ultimate role of APP/Aβ and tau as drivers of neurodegeneration remain undetermined. Mouse models of AD and tauopathy have provided insight into synergistic and independent pathogenic effects of APP and tau (Busche and Hyman, 2020; Puzzo et al., 2020). Mice with mutations in *Mapt* exhibit tau pathology resembling aspects of AD. However, in contrast to our human results, these mice show subtle transcriptional changes and downregulation of synaptic genes (Pickett et al., 2019; Sierksma et al., 2020). This discrepancy may be explained by differences in methodology (i.e., profiling of all cells vs. comparing AT8$^+$ and AT8$^-$ neurons), the cell types exhibiting tau aggregates (i.e., glial and neuronal in tau transgenic models vs. neuronal in human AD), or the potential effects of APP/Aβ on NFT-bearing neurons in AD. Profiling NFT-bearing neurons in AD vs. PART, a primary tauopathy featuring tau aggregates in a similar distribution to AD without amyloid (Crary et al., 2014), could help elucidate the effects and potential synergy of amyloid and tau.

In contrast to the shared dysregulation of synaptic and stress response genes in NFT-bearing neurons, we found that changes in glucose metabolism and mitochondrial function genes were highly cell-type dependent and particularly enriched in Ex3. This cluster differed in the directionality of changes (mostly downregulated in NFT-bearing), pathway enrichment (i.e., ATP metabolic process, oxidative phosphorylation, respiratory electron transport chain), and its TF regulatory networks (i.e., *GABPA*). Intriguingly, this cluster corresponds to a poorly characterized but distinct neuronal subtype in middle cortical layers that expresses *RORB* and *PLCH1* and contains neurons expressing the genes for the neuropeptide galanin (*GAL*) (Alexandris et al., 2019) and neprilysin or CD10 (*MME*). Neprilysin is a transmembrane endopeptidase involved in the cleavage of several neuropeptides, and a major Aβ-degrading enzyme (Farris et al., 2007; Iwata et al., 2001). In neocortex, neprilysin expression has been described in parvalbumin interneurons (Rossier et al., 2015) but its expression by neocortical excitatory neurons was unknown.

We identified a dissociation between NFT susceptibility and neuronal death in the BA9. Although imaging and histopathological studies have demonstrated the regional co-occurrence of NFTs and neurodegeneration, whether NFTs play toxic and/or neuroprotective roles remains debated (Ittner et al., 2016; Kuchibhotla et al., 2014; Menkes-Caspi et al., 2015; Ossenkoppele et al., 2016; Spires-Jones et al., 2008; Wang and Mandelkow, 2016). While we identified notable differences in NFT susceptibility among 20 neuronal subtypes from BA9, we found subtle differences in their susceptibility to death. We replicated this result by re-analyzing two independent snRNA-seq datasets from the same brain region (Leng et al., 2021; Mathys et al., 2019). Other regions including entorhinal cortex and hippocampal CA1 undergo early and substantial neuronal loss (Gómez-Isla et al., 1996). Leng *et al.* showed the early selective vulnerability of *RORB*$^+$ excitatory neurons in Braak II vs. Braak 0 caudal entorhinal cortex. Thus, different brain regions may possess different patterns of vulnerability. Large-scale multi-region and multi-stage single-cell studies are needed to characterize selective vulnerability in greater detail.

Our BA9 results suggest that NFTs may represent cell-type-specific responses to cellular and microenvironmental stressors in AD, and that these responses are neither fully protective nor deadly to the cells bearing them. NFT-bearing neurons showed altered expression of both pro- and anti-apoptotic genes. Although their ultimate effect in survival remains undetermined, upregulation of *ATF4* and other genes involved in the cellular stress response such as *APP, JUN*, and *HSP90AA1* suggests a homeostatic response to cellular injury. This response appears to be insufficient to protect neurons from death in the AD microenvironment, where other factors such as neuroinflammation, hyperexcitable circuits, and vascular pathology (Arboleda-Velasquez et al., 2019; Chen et al., 2020; De Strooper and Karran, 2016; Merlini et al., 2021; Palop and Mucke, 2016) may critically impact neuronal function and survival. Although we cannot distinguish drivers of degeneration from compensatory responses, our datasets provide a resource for exploring tau-dependent and independent pathogenic mechanisms and serve as a platform for discovery.

STAR METHODS

RESOURCE AVAILABILITY

Lead contact—Further information and requests for resources should be directed to and will be fulfilled by the lead contact, Inma Cobos (icobos@stanford.edu).

Materials availability—This study did not generate new unique reagents.

Data and code availability

- Raw single-cell RNA sequencing data generated in this study, associated metadata, and processed digital expression matrices have been deposited at the NCBI's Gene Expression Omnibus with accession number GSE129308. This paper also analyzes existing, publicly available data. The accession numbers for the datasets are listed in the key resources table.
- This paper does not report original code.
- Any additional information required to reanalyze the data reported in this paper is available from the lead contact upon request.

EXPERIMENTAL MODEL AND SUBJECT DETAILS

Human samples—Fresh-frozen human brain samples were obtained from public repositories. Donor demographics and samples characteristics can be found in Table S1. All AD donors used for single-soma transcriptomics (n = 8; 5 females and 3 males) died with dementia and received a neuropathological diagnosis of Alzheimer’s disease neuropathological change, a Braak stage VI of VI, and an ABC score (NIA-AA Research Framework criteria) of A3B3C3 (Hyman et al., 2012; Braak and Braak, 1991). All controls (n = 8; 3 females and 5 males) were cognitively normal and Braak stage 0–II. Donor age ranged from 66 to 93 years (76.9 ± 12.4 and 69.9 ± 7.7 years for AD and controls, respectively [mean ± STD]; not significant change in AD vs. controls; $p = 0.20$; two-sample equal variance t-test). The postmortem interval (PMI) ranged from 1 to 33 hours (12.8 ± 7.6 and 18.2 ± 7.9 hours for AD and controls, respectively [mean ± STD]; not significant change in AD vs. controls; $p = 0.20$; two-sample equal variance t-test). The RNA integrity number (RIN) ranged from 5.7 to 7.8 (6.5 ± 0.4 and 6.9 ± 0.5 for AD and controls, respectively [mean ± STD]; not significant change in AD vs. controls; $p = 0.08$; two-sample equal variance t-test).

METHOD DETAILS

Isolation of individual somas with tau aggregates from frozen human brains —Fresh-frozen brain tissue blocks stored at −80°C were first warmed to −12°C to enable the dissection of thick (~500 μm) tissue sections while preserving the remaining frozen tissue for additional experiments. For each experiment, a section of the cortex (~200 mg) encompassing an equal representation of all cortical layers was cut. The tissue was dissected under a stereomicroscope to remove the white matter and leptomeninges and was then chopped into small pieces (< 1 mm^3) using a chilled razor blade. RNA quality was assessed from ~10 mg of tissue using the RNeasy kit (Qiagen Cat#74134) according to the manufacturer’s instructions to purify RNA, and the Agilent Bioanalyzer 2100 RNA Nano chips (Agilent Technologies Cat#5067-1511) were used according to the manufacturer instructions to quantify the RNA integrity number (RIN). To prevent further RNA degradation during soma isolation, all steps were performed on ice in RNase-free conditions. For tissue homogenization, a Potter-Elvehjem tissue grinder was used. These grinders have a clearance space between the pestle and tubes (0.1-0.15 mm clearance; 8 mL tubes) wider than those of the grinders typically used to dissociate nuclei, which facilitates the dissociation of relatively well-preserved somas. Each tissue sample was dissociated using 2.4 mL of homogenization buffer (10 mM Tris pH 8, 5 mM $MgCl_2$, 25 mM KCl, 250 mM sucrose, 1 μM DTT, 0.5x protease inhibitor [cOmplete Protease Inhibitor Cocktail, MilliporeSigma Cat#11697498001], and 0.2 U/μL RNase inhibitor). No enzymatic digestion or detergents were used. For this amount of tissue, ~15 grinder strokes were needed. The number of strokes was adjusted by microscopically assessing the number and morphology of somas and the presence of clumps using a hemocytometer. Homogenates were then filtered through a 100-μm cell strainer and transferred into two 1.5-mL Eppendorf tubes.

Further clean-up was performed using iodixanol gradient centrifugation. The homogenate was first centrifuged at 400 ×g for 5 min at 4°C. Then, the supernatant was aspirated and discarded, and the pellets were gently resuspended in 200 μL of cold homogenization buffer. The homogenates were pooled into one tube, and the total volume was measured and adjusted with homogenization buffer to obtain an exact volume of 450 μL. An equal volume (450 μL) of 42% v/v iodixanol medium (75 mM sucrose, 25 mM KCl, 5 mM $MgCl_2$, 10 mM Tris [pH 8], and 42% w/v iodixanol) was added to the homogenate and gently mixed with a pipette to obtain a final concentration of 21% iodixanol. The mixture was then transferred to a new 2-mL Eppendorf tube containing 900 μL of cold 25% iodixanol medium (146 mM sucrose, 48 mM KCl, 10 mM $MgCl_2$, 19 mM Tris [pH 8], and 25% w/v iodixanol) by slow layering on the top. The tubes were centrifuged at 8,000 ×g for 15 min at 4°C, resulting in the sedimentation of somas at the bottom, covered by the supernatant and a top layer of thick material containing cell clumps and abundant myelin. The top layer and supernatant were removed and discarded carefully, avoiding contamination of the pellet. Pellets were detached with a small amount (~50 μL) of immunostaining buffer (0.1 M phosphate-buffered saline [PBS; pH 7.4], 0.5% bovine serum albumin [BSA], 5 mM $MgCl_2$, 2 U/mL DNAse I, and 0.2 U/μL RNase inhibitor), transferred to clean tubes, and gently resuspended in a total volume of 200 μL of immunostaining buffer. After a 15-min incubation with immunostaining buffer, at 4°C, with gentle rocking, primary antibodies were added (mouse anti-phospho-Tau [Ser202, Thr205] monoclonal antibody [AT8], 1:150, ThermoFisher Cat#MN1020; rabbit anti-MAP2 polyclonal antibody, 1:40, MilliporeSigma Cat#AB5622), and the suspension was incubated for 40 min at 4°C with gentle rocking. An equal volume (500 μL) of immunostaining buffer was then added, and the tubes were inverted several times before being centrifuged at 400 ×g for 5 min at 4°C. The supernatant was carefully removed, and the pellets were resuspended in 600 μL of immunostaining buffer. Secondary antibodies (goat-anti-mouse, Alexa Fluor 350, 1:500; goat-anti-rabbit, Alexa Fluor 647, 1:500) and a nuclear stain (SYTOX green, 1:40,000) were added, and the solutions were incubated for 30 min at 4°C with gentle rocking. Aliquots of unstained, secondary antibody-treated only, and single-stained (SYTOX green, MAP2, or AT8) cells were saved as FACS controls.

The number and morphology of the somas were evaluated microscopically after each critical step and immediately before FACS. Good-quality samples contained a suspension of single somas and naked nuclei, with few clumps and little debris; the proportion of cells with relatively well-preserved somas varied between 20-50% of the total sample. The typical yield for ~100 mg of cerebral cortex tissue was between 0.5–1.5 × 10^6 somas.

FACS of somas with and without NFTs—FACS was used to collect single-cell suspensions of somas with tau aggregates. Sorting was performed using a BD FACS Aria II at the Flow Cytometry Core Laboratory at UCLA or a Sony SH800S equipped with four excitation lasers (488nm, 405nm, 638nm and 561nm) at Stanford. We tested three antibodies against pathological tau that recognize different stages of NFT maturity: AT8, T22 and PHF1 (Moloney et al., 2021). AT8 (mouse anti-phospho-Tau [Ser202, Thr205] monoclonal antibody; ThermoFisher Cat#MN1020) is the standard antibody in Neuropathology for clinical and research applications and a marker for both pretangles and mature tangles; T22 (rabbit polyclonal anti oligomeric tau [T22]; MilliporeSigma Cat#ABN454) is an antibody against oligomeric tau; PHF1 (rabbit anti-phospho-Tau [Ser396] monoclonal antibody; Abcam Cat#ab109390) is enriched in mature and ghost tangles. Suspensions of single somas isolated from the BA9 of Braak VI AD donors (n = 4) were co-stained with AT8 and either T22 or PHF1, analyzed by FACS, and collected for microscopic examination (Figure S2).

We selected AT8 for the isolation and profiling of neurons with pathological tau aggregates. We collected single-cell suspensions of somas with tau aggregates ($AT8^+$) and neighboring neurons without tau aggregates ($MAP2^+/AT8^-$) from AD brains as well as neuronal somas ($MAP2^+$) from control brains. PBS was used as the sheath fluid, with a sheath pressure of 20 psi. A 100-μm nozzle tip was used, and the frequency of droplet generation was ~30 kHz. The primary laser was a blue Trigon 488-nm used in the generation of forward scatter (FSC) and side scatter (SSC). The secondary lasers were UV Trigon 355-nm, blue Trigon 488-nm, and red Trigon 640-nm, used for the excitation of Alexa 350, SYTOX green, and Alexa Fluor 647, respectively. Sample events were acquired at < 30% droplet occupancy.

FACS gates were based on a combination of regions drawn around target populations in 2D plots, performed in the following order: FSC height vs. SSC height; SSC area vs. FSC width; FSC area vs. FSC width; SSC area vs. SYTOX green fluorescence (bandpass filter 525/50); and Alexa 350 fluorescence (bandpass filter 450/50) vs. Alexa Fluor 647 fluorescence (bandpass filter 670/30). The FSC versus SSC gates were set with permissive limits, discarding the smallest and largest particles. SYTOX green fluorescence was used to discriminate single cells from cell clumps and anucleated cell fragments. Alexa Fluor 647 was used to discriminate neurons with soma ($MAP2^+$) from nonneuronal cells and naked neuronal nuclei ($MAP2^-$). Alexa Fluor 350 was used to discriminate between somas containing tau aggregates ($AT8^+$) and somas without tau aggregates ($AT8^-$). Unstained, only secondary antibody-treated, and only single primary antibody-treated cell suspensions were included as controls to minimize false positives due to nonspecific staining or autofluorescence.

Two populations from AD brains were collected: $AT8^+$ (either positive or negative for MAP2) and $MAP2^+/AT8^-$ somas; a population of $MAP2^+$ somas was collected from control brains. The yield per sample ranged from 1,600–37,000 somas for $AT8^+$ and over 3×10^5 somas for $MAP2^+$. Somas were collected in 1.5-mL Eppendorf tubes containing 100–200 μL of collection buffer (0.1 M PBS [pH 7.4] and 0.1 U/μL RNase inhibitor). After collection, BSA was added to each tube for a final concentration of 1%. To prevent somas from adhering to the tube walls, the Eppendorf tubes used for collection were precoated with

BSA. BSA precoating was performed by filling the tubes with 10% BSA solution in PBS for 5 min, rinsing with PBS, and drying at 4°C overnight.

Western blotting of FACS-sorted somas—Somas with and without NFTs were collected by FACS in 0.1 M PBS (30,000–400,000 somas per sample), and the pellets lysed in RIPA buffer (Cell Signaling Technology, Cat#9806S) in the presence of cOmplete Protease Inhibitor Cocktail (MilliporeSigma Cat#11697498001). Total protein concentration was quantified using a Bradford protein assay in duplicate. Samples were separated on 4-20% Mini-PROTEAN TGX Gels (Bio-Rad Cat#4561094) and then transferred to PVDF membranes (Bio-Rad Cat#10026934). Membranes were blocked with 5% skimmed milk in Tris Buffered Saline + 0.1% Tween 20 (TBST) and incubated with anti-SQSTM1/p62 antibody (1:1000, Abcam Cat#ab109012) at 4°C overnight, and then washed and incubated with horseradish peroxidase-conjugated (HRP) conjugated secondary antibody for 1 hour at RT. Membranes were visualized with ECL substrate (ThermoFisher Cat#32209). To control for loading, the membranes were stripped with Blot Stripping Buffer (ThermoFisher Cat#46430) and reprobed with the following antibodies: anti-beta Actin (1:25000, Abcam Cat#ab49900), anti-Lamin B1 (1:1000, Cell Signaling Technology Cat#12586), and anti-Histone H3 (1:5000, EpiCypher Cat#13-0001).

Single-soma RNA-sequencing—Single-soma mRNA capture and library preparation were performed using the 10x Genomics Chromium Single Cell 3' v2 or v3 assays. Single-cell suspensions for FACS were centrifuged at 400 ×g for 5 min at 4°C to concentrate cells. Without disturbing the pellet, sufficient supernatant was removed to achieve a concentration of ~350 cells per μL. Cell concentrations were measured using a hemocytometer, and the quality of cells was examined under a fluorescence microscope. The numbers of loaded cells ranged from 1,400–11,000 to capture the maximum number of cells, with an upper limit of ~5,000 cells per sample (for an expected cell capture efficiency of ~40%). The following steps were performed according to the manufacturer's instructions. For cDNA amplification, the number of PCR cycles used was 13–15 (adjusted to the targeted cell recovery). For library construction, the number of cycles for the sample index PCR was 12–13 (adjusted for the quantified cDNA input).

The generated paired-end libraries were sequenced on Illumina Novaseq 6000. All the libraries from the AD donors were combined and sequenced together in a single run. The concentration of each sample was normalized to the total number of cells to achieve similar numbers of reads per cell. Cells were sequenced at a depth of ~72,000 reads per cell, corresponding to a sequencing saturation of ~85%.

Paired-end sequence reads were processed using the 10x Genomics software package Cell Ranger version 3.1. We used the Cell Ranger count pipeline with default parameters to perform alignment to the prebuilt reference genome GRCh38 and for filtering, barcode counting, and UMI counting. The resulting digital expression matrices were analyzed using the R-based Seurat package, versions v2, v3, or v4.

Analysis of the AT8$^-$, AT8$^+$, and combined AT8$^-$ and AT8$^+$ datasets—To analyze the AT8$^-$ datasets, we loaded all digital expression matrices into Seurat, filtered out cells with < 250 genes or > 12,000 UMIs, and removed mitochondrial DNA-encoded genes, ribosomal genes, and uncharacterized RP11-, RP13-, RP1-, RP3-, RP4-, RP5-, and RP6-genes. All datasets were combined and normalized using the function LogNormalize with the default scale factor 10,000. The number of UMIs and samples of origin were regressed out. We selected genes with average expression values between 0.0075 and 3 and dispersion values > 0.3 (~4,200 genes) for downstream analysis. Principle component analysis (PCA) was used to reduce dimensionality, and the first 22 statistically significant principal components (PCs) were selected for clustering. Clusters were identified using a graph-based clustering approach (Seurat FindClusters function with the following parameters: 1:22 PCs; 1.0 resolution; 100 random start positions and 10 iterations per random start; and 30 k for the k-nearest neighbor algorithm) and visualized with t-SNE using the same PCs. Cluster-specific marker genes were obtained by comparing the gene expression levels for each individual cluster with those for all other cells using the Wilcoxon rank-sum and MAST tests. Genes detected in ≥ 25% of cells (in either the tested cluster or in all other cells combined) with positive log-fold changes > 0.25 and adjusted p-values < 0.05 were included. Cluster robustness was assessed by examining cluster stability after subsetting and rerunning clustering and by comparing our data with previous human brain snRNA-seq (Hodge et al., 2019; Mathys et al., 2019) and gene expression data. We annotated 23 clusters corresponding to 13 excitatory neuron subtypes, 7 inhibitory neuron subtypes, and 3 glial cell types. Clusters containing cells with mixed identities and/or cell states (1.57%; gray colored) were removed from further analysis.

To analyze the AT8$^+$ datasets and the combined AT8$^-$ and AT8$^+$ datasets, we used multiCCA for dimensionality reduction (Butler et al., 2018). MultiCCA performed better than PCA in distinguishing between cell types and disease states. We used the same parameters as described above to filter low-quality cells, except that we regressed out mitochondrial DNA-encoded genes instead of filtering them. The top 4,200 highly variable genes that were present in at least two datasets were selected for downstream analysis. The first 26 canonical correlation vectors were aligned using the datasets/samples as a grouping variable (Figures S4G-J). Clustering and t-SNE were performed using the same canonical correlation and a resolution of 1. Cluster-specific marker gene identification and cluster robustness assessment were performed as described above.

To further assess the robustness of the clustering of the combined AT8$^-$ and AT8$^+$ datasets, we reanalyzed our sequencing data after alignment to a pre-mRNA reference genome (Figure S3). This approach has been shown to markedly improve gene detection in nuclear preparations due to the high fraction of intronic reads captured in nuclear sequencing (Bakken et al., 2018). We created a custom pre-mRNA reference package by modifying the prebuilt reference genome GRCh38 provided by Cell Ranger to include both intronic and exonic reads for downstream analysis. The resulting digital expression matrices were analyzed using version v3.1 of the R-based Seurat package. We used the single-cell transform (SCT) method for normalization, variance stabilization, regression of the number of UMIs and mitochondrial gene fraction (Hafemeister and Satija, 2019), and uniform manifold approximation and projection (UMAP) for dimensionality reduction and clustering. By selecting the first 6 statistically significant PCs, we first obtained three clusters corresponding to excitatory neurons, inhibitory neurons, and nonneuronal cells.

Subsequently, we performed an independent clustering analysis for the excitatory neuron and inhibitory neuron subsets. Identification of cluster-specific marker genes and cluster annotation was performed as described above.

Analysis of the non-AD, AD-AT8$^-$ and AD-AT8$^+$ datasets—To analyze the non-AD (healthy controls), AD-AT8$^-$, and AD-AT8$^+$ datasets together, we generated two sets of digital expression matrices from each sample, after alignment to exons (prebuilt reference genome GRCh38 provided by Cell Ranger version 3.1) or to our custom pre-mRNA reference (built by modifying the prebuilt reference genome in Cell Ranger to include both intronic and exonic reads) and integrated both into a single Seurat object. The reads aligned to pre-mRNA were used for clustering, and the reads aligned to exons were used for DGE analyses.

We used SCT for multidataset integration and UMAP for dimensionality reduction and clustering using Seurat versions v3 and v4. SCT integration was performed after splitting the combined dataset into different objects based on a combination of two variables, sorting (AT8$^+$ or AT8$^-$) and sequencing chemistry (10x Genomics v2 or v3), and then applying the sctransform function, which incorporates normalization, scaling and identifying highly variable genes (top 3000 genes) while regressing out two unwanted sources of variation, the total number of UMIs and the percentage of mitochondrial genes per sample.

For clustering, we first subset the clusters corresponding to excitatory or inhibitory neurons identified after running UMAP, FindNeighbors and FindClusters with default parameters and using the first 10 statistically significant PCs. We then performed an independent clustering analysis for the excitatory neuron and inhibitory neuron subsets with higher resolution parameters. We used the R-based package Clustree version 0.4.4 to visualize the clustering at different resolutions from 0.1 to 1.0. Identification of cluster-specific marker genes and cluster annotation was performed as described above.

Single-cell reference mapping and annotation of published datasets—To compare the neuronal composition of the BA9 across single-cell AD datasets (Figure S8), we used the neuronal subtype annotations from our BA9 control dataset as reference (Figure S1; neuronal nuclei and somas; 64,792 cells after QC) to reanalyze and annotate our single-soma AD dataset (Figure 7) and two published single-nucleus datasets (Leng et al., 2021; Mathys et al., 2019) using the function MapQuery in the Seurat package version v4. The published query datasets were downloaded from Synapse (Mathys *et al.*: https://www.synapse.org/#!Synapse:syn18485175) and Cellxgene (Leng *et al.*: https://cellxgene.cziscience.com/collections/180bff9c-c8a5-4539-b13b-ddbc00d643e6). For each of the published query datasets, we subset the excitatory and inhibitory neurons as annotated by the authors and kept only the nuclei that passed the QC parameters set by the authors (44,123 neuronal nuclei in Mathys *et al.* and 23,339 neuronal nuclei in Leng *et al.*).

First, we used the function FindTransferAnchors in Seurat v4 to define a set of anchors between the reference and each of the three query objects (default parameters with SCT as normalization method and PCA for dimensional reduction with 50 dimensions). Then, we computed a reference UMAP model (RunUMAP function with default parameters and the first 25 dimensions) from our BA9 control dataset as a reference for cluster annotations. Finaly, we used the wrapper function MapQuery to predict the identity of the query cells and to transfer the annotations from the reference to the query datasets (TransferData function), integrate the datasets using the pre-computed set of anchors (IntegrateEmbeddings function), and project the query datasets onto the reference UMAP (ProjectUMAP function, a wrapper for FindNeighbors and RunUMAP).

Statistical analysis of NFT and cell death susceptibility—To test for statistically significant differences in cell composition among datasets (i.e., AD vs. non-AD in Figure 7, comparisons across published single-cell AD datasets in Figure S8, and comparisons between nuclear and soma isolation methods in Figure S1), we obtained the relative abundance of each neuronal subtype for each donor, on a scale from 0 to 1, either relative to all neurons or to either excitatory or inhibitory neurons separately and performed beta regression using the R package betareg version 3.1-4. We used the formula Relative.Abundance ~ Condition with the bias-corrected maximum likelihood estimator (R>betareg(Relative.Abundance ~ Condition, data=data ,type="BC")). To correct for multiple hypothesis testing, we used Holm's method to adjust the *p* values obtained from beta regression using the p.adjust function of the R Stats package with the number of neuronal subtypes tested as the "length" variable.

For the AT8$^+$ vs. AT8$^-$ comparison, where both AT8$^+$ and AT8$^-$ cells were obtained from the same donor, we added random effects to the model to account for the paired design. We fitted a generalized linear mixed model using maximum likelihood estimation via 'TMB' (Template Model Builder) with the R package glmmTMB, using the formula Relative.Abundance ~ AT8.condition + (1|Donor), and the function "beta_family". Correction for multiple hypothesis testing was performed as described above.

DGE analysis—DGE between NFT and NFT-free and between non-AD and AD datasets was assessed using the MAST generalized linear model (Finak et al., 2015) on each cluster separately (Tables S2 and S6). MAST considers the characteristic bimodal distribution of single-cell data in which gene expression is either detected (nonzero) or not detected (typically high due to the high rate of dropout events). It has been shown to perform highly favorably on statistical power and FDR control compared to other methods for DGE analysis in single-cell datasets (Soneson and Robinson, 2018). To generate the lists of DE genes, we applied MAST using the Seurat function FindMarkers (Seurat v4). The following parameters and cut-off values were included in the design formula: adjusted p-value < 0.05 (based on Bonferroni correction using the total number of genes in the dataset); log2 fold change (positive or negative) > 0.2; detection in ≥ 20% of cells for at least one condition; and nUMI (i.e., cellular detection rate), age, sex, and RIN as latent variables (i.e., cofounding variables).

To visualize shared and distinct DE genes across cell types with or without NFTs, we generated gene expression heatmaps by hierarchical clustering of genes using Ward’s minimum variance method with the heatmap.2 R package. The resulting clustering was used to build the row (genes) dendrogram. Columns (cell types) were clustered using Euclidian distance and reordered by mean values.

Cross-validation of the molecular signatures associated with NFTs was performed by rerunning DGE after excluding a subset of samples. We removed different combinations of two of the eight samples from the dataset, generated full lists of DE genes using MAST, and compared them with the lists of DE genes generated from the 8-sample dataset. We used the RRHO (Plaisier et al., 2010) to identify and visualize statistically significant overlap between pairs of gene lists (RRHO 1.22.0 R package). The full lists of genes without any cut-off filters were ranked by their adjusted p-values, and the statistical significance of the number of overlapping genes was measured successively to determine the strength and pattern of correlations. The output was visualized using heatmaps with a step size (i.e., resolution) of 50 (Figure S4).

TFBS analysis—Transcription factor binding site (TFBS) enrichment analysis was performed in the promoters of the genes that were DE in cells with NFTs, compared to cells that were NFT free in five neuronal subtypes (Ex1, Ex2, Ex3, Ex7, Ex10), using the TFBS pipeline described elsewhere (Parikshak et al., 2016). The region 1 kb upstream of the transcription start site was defined as the canonical promoter region. For each of the five clusters, we assessed the top 200 connected genes, ranked by intramodular connectivity (kME), using the Religious Orders Study and Memory and Aging Project (ROSMAP) prefrontal cortex AD dataset (Mostafavi et al., 2018). Putative motifs bound by the TF were obtained from the TRANSFAC database (Matys et al., 2003). We identified the upstream sequences of these 200 genes using the Clover algorithm (Frith et al., 2004) to calculate motif enrichment. The background for enrichment was calculated with the MEME algorithm (Bailey and Elkan, 1994) using 1000-bp sequences upstream of all human genes, human CpG islands, and the sequence of human chromosome 20. We calculated p-values by selecting 1,000 sequences of the same length, testing them for enrichment using MEME, and computing the p-values based on the observed motif enrichment ranks versus the randomized sets. The enriched TFs for each of the five neuronal subtype clusters were obtained (Figure S5).

TF regulatory networks—To generate neuronal TF regulatory networks, we obtained data for human neuronal TFs and their target genes from the ENCODE ChIP-seq dataset (Consortium, 2012; Davis et al., 2018) and intersected them with the TFs identified in our TFBS enrichment analysis. For each TF regulatory network, we defined the genes with robust evidence of coexpression across brain tissues based on AMP-AD network analysis using the top 100 connected genes (ranked by kME) for each coexpression module (Morabito et al., 2020) the genes that were DE in cells with NFTs versus NFT-free cells (Table S2), and cluster-specific background genes (expressed in ≥ 10% of cells in the cluster). The edges in the networks represent the bicorrelation of gene expression values in the AMP-AD datasets, and the nodes are spatially arranged by multidimensional scaling (MDS) of the AMP-AD gene expression. In the interest of visual clarity of the networks, we limited the genes displayed to a maximum of 25 DE genes (ranked by p-value) and 20 background genes (ranked by p-value); the numbers of DE genes between NFT versus NFT-free cells that were also coexpressed in the AMP-AD network analysis were not limited (Figure S5B). The complete list of genes and intramodular connectivity data for each transcriptional regulatory network are provided in Table S3.

GO enrichment analysis—The web server g:Profiler (version Ensembl 97, Ensembl Genomes 44) (Raudvere et al., 2019) was used to perform GO enrichment analysis. To analyze the NFT-bearing and NFT-free somas, we input for each cluster the list of DE genes between cells with and without NFTs against a list of background genes (expressed in ≥ 10% of cells in the cluster) and obtained hierarchical sorting lists of GO terms. Statistical significance thresholds were determined using Fisher's exact test and multiple testing correction (default native method g:SCS). To limit the size of functional categories subjected to enrichment analysis, we filtered out GO terms with < 50 or > 500 genes. Data were downloaded in generic enrichment map (GEM) format to be used as input for functional enrichment analysis. Cytoscape with EnrichmentMap (Merico et al., 2010) was used to integrate and visualize GO enrichment results from the five excitatory clusters with the highest cell numbers and percentages of $AT8^+$ cells into a single network. The ranked lists of statistically significant GO biological process terms obtained with g:Profiler were loaded into Cytoscape v3.8.2 with the EnrichmentMap app. v3.2 using the following conservative parameters: nodes (representing GO-derived gene sets) included gene sets with p-values < 0.02 and FDR q-values <0.1; edges (representing gene overlap between gene sets) used an overlap coefficient threshold of 0.7. Each of the five clusters was color coded to visualize the shared and distinct contributions of each cell type. The enrichment map was annotated automatically using the Autoannotate app. and the clusters labeled with three words using the WordCould app. To analyze together AD-associated and NFT-associated enrichment, we followed the same workflow to first generate hierarchical sorting lists of GO terms (AD-associated: DE genes between AD-$AT8^-$ and non-AD; NFT-associated: DE genes between AD-$AT8^+$ and AD-$AT8^-$) and then integrate the two comparisons into a single network for each cluster (Ex1, Ex2, Ex3, Ex7, Ex10).

The SynGO enrichment tool (Koopmans et al., 2019) was used to further characterize the synaptic transmission pathways enriched in neurons with NFTs. The list of genes associated with synaptic transmission by functional enrichment analysis (genes in clusters #1, #2 and #6 in Table S4; 510 genes) was loaded against a custom background list containing all genes expressed in the five excitatory cell subtypes analyzed (6,843 genes; expressed in ≥ 10% of cells). Using high-stringency parameters to filter annotations by experimental evidence and a minimum of 3 matching input genes per term, 227 genes mapped to SynGO annotated categories; 171 genes had a cellular component annotation, and 176 genes had a biological process annotation. A total of 24 cellular component and 39 biological process terms were significantly enriched at 1% FDR.

Histological validation in human brain tissue—Validation of selected gene markers was performed in the BA9 from the same AD donors used for transcriptomics. Single and double chromogenic RNAscope ISH staining was performed on 20-μm-thick cryosections from fresh-frozen tissue following the manufacturer's protocol (RNAscope 2.5 HD assay and duplex assay). Human RNAscope probes were obtained from ACD Bio. to detect the following genes: *SLC17A7* (#415611), *GAD1* (#404031), *CUX2* (#425581), *LAMP5* (#487691), *COL5A2* (#510911), *RORB* (#446061), *GAL* (#317631), *GABRG1* (#485931), *RPRM* (#565701), *PCP4* (#446111), *ROBO3* (#483191), *NR4A2* (#582621), and *NTNG2*

(#551651). Adjacent Nissl-stained and NeuN-immunostained sections served as anatomical references to delineate boundaries between cortical layers.

Quantification of the proportions of neurons with NFTs within neocortical layers was performed on 20-μm-thick cryosections immunostained with NeuN (mouse anti-NeuN antibody, 1:1,000, MilliporeSigma Cat#MAB377) and p-tau Thr205 (rabbit anti-p-tau Thr205, 1:1000, ThermoFisher Cat#44-738G) and counterstained with DAPI (8 donors). Quantification of the proportions of neurons with NFTs in specific neuronal subtypes was performed by double or triple fluorescent AT8 IHC and RNAscope ISH for cell identity markers (*SLC17A7, GAD1, CUX2, PCP4, ROBO3, NR4A2, NTNG2*) on 12-μm-thick sections (4 donors). Prior to staining, the sections were photobleached to quench lipofuscin autofluorescence using an LED light source (Sun et al., 2017). For this, sections were fixed in 4% paraformaldehyde for 15 min at 4°C, washed twice in 1x PBS for 5 min, and then exposed to an LED light source (300-watt, full spectrum LED; Platinum LED Lights, Cat# P300). Sections were kept in 1x PBS, placed at a distance of 40 cm from the LED, and exposed for 36–48 hours at 4°C. After photobleaching, RNAscope ISH was performed using the Multiplex Fluorescent Reagent Kit v2 according to the manufacturer's instructions, except for a shortened protease treatment time of 15 min. Fluorescence signals were amplified and visualized using the TSA Plus Cyanine-5 and the TSA Plus Fluorescein systems (Akoya Biosciences, #NEL745E001KT and #NEL741E001KT, respectively), according to the manufacturer's instructions, using a TSA Plus working solution concentration of 1:500. After ISH, the sections were fixed in 4% paraformaldehyde for 15 min at 4°C and then washed twice in 1x PBS for 5 min. Nonspecific binding was blocked with 10% normal goat serum in PBS for 30 min at 4°C. Sections were then incubated with 1:100 AT8 antibody in 1x PBS with 5% normal goat serum at 4°C overnight. The next day, the sections were washed three times for 10 min in 1x PBS and incubated with 1:50 goat anti-mouse Alexa Fluor 350 for 1 hour at 4°C. Sections were washed in 1x PBS three times for 5 min and mounted with Vectashield antifade mounting medium (Vector Laboratories).

We used digital images taken at 400x magnification with a Zeiss Axio Imager M2 microscope equipped with a monochrome digital camera (Hamamatsu C11440-22CU) and the Zeiss ApoTome.2 optical sectioning system to quantify the colocalization of AT8 with the different neuronal subtype markers. Multiple images were acquired automatically within a region of interest that was traced manually to include the entire thickness of the cortex (for *SLC17A7* and *GAD1*), the upper layers 2-3 (for *CUX2*), the middle layers 3b-5 (for *PCP4*), layer 5b (for *PCP4* and *ROBO3*), or layer 6 (for *NTNG2* and *NR4A2*) and then combined into a single image using the slide-scanning module in Stereo Investigator software v.2018 (MBF Bioscience). A total of 10–12 counting frames (400 μm x 250 μm) were randomly placed within the region of interest to cover an area of ~5 mm^2. Double- or triple-positive cells were counted manually using the Placing markers module in Stereo Investigator. For *PCP4/ROBO3/*AT8 triple staining, cells were counted throughout layer 5b (7.5 to 15 mm2). Four patients and ≥ 2 sections per marker were analyzed. The investigator was blinded to the sample and to the results obtained from single-cell RNA-seq studies. A total of 1,200–5,000 cells per marker were analyzed. The results are expressed as the percentage of double- or triple-positive cells and the standard deviation for each gene marker.

The quantification of synaptic markers and *ATF4* expression levels in excitatory neurons with and without NFTs was performed by double AT8 IHC and RNAscope ISH (Multiplex Fluorescent Reagent Kit v2) for *SLC17A7* combined with either *SNAP25*, *GABRA1, GRIN2B, SYT1, or ATF4* (ACD Bio. probe numbers #518851, #472141, #485851, #525791, and #405741 respectively), on 12-µm-thick sections from 4 AD donors (2 sections each). The sections were photobleached to quench lipofuscin autofluorescence, immunostained for AT8 and processed for RNAscope ISH as described above, then counterstained with DAPI. Four-channel image acquisition was performed at 200x magnification using a Zeiss Axio Imager M2 microscope equipped with a monochrome digital camera (Hamamatsu C11440-22CU) and the Zeiss ApoTome.2 optical sectioning system. Each area of acquisition was selected using the slide-scanning module in the Stereo Investigator software v.2018 (MBF Bioscience) within a region of interest traced manually to include layers 2-3.

Images were processed using ImageJ (Fiji v.2.3.1). First, individual cells were identified via segmentation of the DAPI images using the watershed function with default parameters. Nuclei were filtered by size to exclude cell fragments and clumped nuclei. Then, the integrated density (IntDen; defined as the product of area and mean grey value of each region of interest) of each RNA probe was calculated and recorded within each cell (~5,000–15,000 cells per marker). Non-excitatory neurons were filtered out by eliminating cells with a *SLC17A7* IntDen value below a threshold ranging from 0.12 to 0.4 by sample. Similarly, cells were sorted into $AT8^{-}$ and $AT8^{+}$ populations by identifying an AT8 IntDen threshold for tau-positive cells in each case. To assess expression level differences of *SNAP25, GABRA1, GRIN2B* and *SYT1* between $AT8^{-}$ and $AT8^{+}$ cells, we compared the mean IntDen of each gene from the $AT8^{-}$ and $AT8^{+}$ populations for each sample and gene after fitting a Linear Mixed Model with IntDen as dependent variable, AT8 as independent pseudo-variable ($AT8^{+}$, $AT8^{-}$), and "sample" as a random effect with the formula IntDen ~ AT8 + (1lsample). Outliers due to imaging artifacts were excluded from the analysis using the R function rstatix::identify_outliers(IntDen).

QUANTIFICATION AND STATISTICAL ANALYSIS

Statistical analyses were performed using R version 4.0.2 or GraphPad Prism version 9 (GraphPad, San Diego, CA). The number of donors, tissue sections, or cells and *p* values for each experiment are noted in the figure legends. Statistical details of each experiment are included in the Method details section.

ADDITIONAL RESOURCES

- The datasets are publicly available for interactive viewing and exploration on the cellxgene platform by the Chan Zuckerberg Initiative at https://cellxgene.cziscience.com/collections/b953c942-f5d8-434f-9da7-e726ba7c1481
- The single-soma isolation protocol is publicly available at https://www.protocols.io/view/isolation-of-single-somas-from-postmortem-fresh-fr-bp2l64o2dvqe/v1

Supplementary Material

Refer to Web version on PubMed Central for supplementary material.

ACKNOWLEDGMENTS

Human tissue was obtained from UCLA-Easton Center, NIH Neurobiobank (Sepulveda repository, Los Angeles, CA, and Mount Sinai, New York, NY), and the Stanford Alzheimer Disease Research Center (NIH/NIA P30 AG066515) with assistance from Abel Nunez, Spencer Tung, and Kazu Williams. FACS was performed at the UCLA Jonsson Comprehensive Cancer Center Flow Cytometry Core Facility. 10x Genomics and sequencing was performed at the UCLA Technology Center for Genomics & Bioinformatics. Supported by grants from NIH/NIA (R01AG059848), BrightFocus (A20173465), Alzheimer’s Association (AARG-17-528298), and Chan Zuckerberg Initiative (Ben Barres Early Career Acceleration Award; grant ID 199150) to I.C., American Federation of Aging Research (AFA-5550485) to V.S., a gift from David and Diane Steffy to W.E.L. and I.C., and UCI MCSB graduate program to S.M.

REFERENCES

Alexandris AS, Walker L, Liu AKL, McAleese KE, Johnson M, Pearce RKB, Gentleman SM, and Attems J (2019). Cholinergic deficits and galaninergic hyperinnervation of the nucleus basalis of Meynert in Alzheimer's disease and Lewy body disorders. Neuropathol Appl Neurobiol. 10.1111/nan.12577.

Arboleda-Velasquez JF, Lopera F, O'Hare M, Delgado-Tirado S, Marino C, Chmielewska N, Saez-Torres KL, Amarnani D, Schultz AP, Sperling RA, et al. (2019). Resistance to autosomal dominant Alzheimer's disease in an APOE3 Christchurch homozygote: a case report. Nat Med 25, 1680–1683. 10.1038/s41591-019-0611-3. [PubMed: 31686034]

Bailey TL, and Elkan C (1994). Fitting a mixture model by expectation maximization to discover motifs in biopolymers. Proc Int Conf Intell Syst Mol Biol 2, 28–36. [PubMed: 7584402]

Bakken TE, Hodge RD, Miller JA, Yao Z, Nguyen TN, Aevermann B, Barkan E, Bertagnolli D, Casper T, Dee N, et al. (2018). Single-nucleus and single-cell transcriptomes compared in matched cortical cell types. PLoS One 13, e0209648. 10.1371/journal.pone.0209648. [PubMed: 30586455]

Ballatore C, Lee VM, and Trojanowski JQ (2007). Tau-mediated neurodegeneration in Alzheimer's disease and related disorders. Nat Rev Neurosci 8, 663–672. 10.1038/nrn2194. [PubMed: 17684513]

Bejanin A, Schonhaut DR, La Joie R, Kramer JH, Baker SL, Sosa N, Ayakta N, Cantwell A, Janabi M, Lauriola M, et al. (2017). Tau pathology and neurodegeneration contribute to cognitive impairment in Alzheimer's disease. Brain 140, 3286–3300. 10.1093/brain/awx243. [PubMed: 29053874]

Braak H, and Braak E (1991). Neuropathological stageing of Alzheimer-related changes. Acta Neuropathol 82, 239–259. [PubMed: 1759558]

Braak H, and Del Tredici K (2015). The preclinical phase of the pathological process underlying sporadic Alzheimer's disease. Brain 138, 2814–2833. 10.1093/brain/awv236. [PubMed: 26283673]

Braak H, and Del Tredici K (2018). Spreading of Tau Pathology in Sporadic Alzheimer's Disease Along Cortico-cortical Top-Down Connections. Cereb Cortex 28, 3372–3384. 10.1093/cercor/bhy152. [PubMed: 29982389]

Brinkmalm A, Brinkmalm G, Honer WG, Frölich L, Hausner L, Minthon L, Hansson O, Wallin A, Zetterberg H, Blennow K, and Öhrfelt A (2014). SNAP-25 is a promising novel cerebrospinal fluid biomarker for synapse degeneration in Alzheimer's disease. Mol Neurodegener 9, 53. 10.1186/1750-1326-9-53. [PubMed: 25418885]

Busche MA, and Hyman BT (2020). Synergy between amyloid-β and tau in Alzheimer's disease. Nat Neurosci 23, 1183–1193. 10.1038/s41593-020-0687-6. [PubMed: 32778792]

Busche MA, Wegmann S, Dujardin S, Commins C, Schiantarelli J, Klickstein N, Kamath TV, Carlson GA, Nelken I, and Hyman BT (2019). Tau impairs neural circuits, dominating amyloid-β effects, in Alzheimer models in vivo. Nat Neurosci 22, 57–64. 10.1038/s41593-018-0289-8. [PubMed: 30559471]

Bussière T, Giannakopoulos P, Bouras C, Perl DP, Morrison JH, and Hof PR (2003a). Progressive degeneration of nonphosphorylated neurofilament protein-enriched pyramidal neurons predicts cognitive impairment in Alzheimer's disease: stereologic analysis of prefrontal cortex area 9. J Comp Neurol 463, 281–302. 10.1002/cne.10760. [PubMed: 12820162]

Bussière T, Gold G, Kövari E, Giannakopoulos P, Bouras C, Perl DP, Morrison JH, and Hof PR (2003b). Stereologic analysis of neurofibrillary tangle formation in prefrontal cortex area 9 in aging and Alzheimer's disease. Neuroscience 117, 577–592. 10.1016/s0306-4522(02)00942-9. [PubMed: 12617964]

Butler A, Hoffman P, Smibert P, Papalexi E, and Satija R (2018). Integrating single-cell transcriptomic data across different conditions, technologies, and species. Nat Biotechnol. 10.1038/nbt.4096.

Canchi S, Raao B, Masliah D, Rosenthal SB, Sasik R, Fisch KM, De Jager PL, Bennett DA, and Rissman RA (2019). Integrating Gene and Protein Expression Reveals Perturbed Functional Networks in Alzheimer's Disease. Cell Rep 28, 1103–1116.e1104. 10.1016/j.celrep.2019.06.073. [PubMed: 31340147]

Cao X, and Südhof TC (2001). A transcriptionally [correction of transcriptively] active complex of APP with Fe65 and histone acetyltransferase Tip60. Science 293, 115–120. 10.1126/science.1058783. [PubMed: 11441186]

Chen WT, Lu A, Craessaerts K, Pavie B, Sala Frigerio C, Corthout N, Qian X, Laláková J, Kühnemund M, Voytyuk I, et al. (2020). Spatial Transcriptomics and In Situ Sequencing to Study Alzheimer's Disease. Cell 182, 976–991.e919. 10.1016/j.cell.2020.06.038. [PubMed: 32702314]

Consortium EP (2012). An integrated encyclopedia of DNA elements in the human genome. Nature 489, 57–74. 10.1038/nature11247. [PubMed: 22955616]

Crary JF, Trojanowski JQ, Schneider JA, Abisambra JF, Abner EL, Alafuzoff I, Arnold SE, Attems J, Beach TG, Bigio EH, et al. (2014). Primary age-related tauopathy (PART): a common pathology associated with human aging. Acta Neuropathol 128, 755–766. 10.1007/s00401-014-1349-0. [PubMed: 25348064]

Darmanis S, Sloan SA, Zhang Y, Enge M, Caneda C, Shuer LM, Hayden Gephart MG, Barres BA, and Quake SR (2015). A survey of human brain transcriptome diversity at the single cell level. Proc Natl Acad Sci U S A 112, 7285–7290. 10.1073/pnas.1507125112. [PubMed: 26060301]

Davidsson P, Jahn R, Bergquist J, Ekman R, and Blennow K (1996). Synaptotagmin, a synaptic vesicle protein, is present in human cerebrospinal fluid: a new biochemical marker for synaptic pathology in Alzheimer disease? Mol Chem Neuropathol 27, 195–210. 10.1007/BF02815094. [PubMed: 8962603]

Davis CA, Hitz BC, Sloan CA, Chan ET, Davidson JM, Gabdank I, Hilton JA, Jain K, Baymuradov UK, Narayanan AK, et al. (2018). The Encyclopedia of DNA elements (ENCODE): data portal update. Nucleic Acids Res 46, D794–D801. 10.1093/nar/gkx1081. [PubMed: 29126249]

De Strooper B, and Karran E (2016). The Cellular Phase of Alzheimer's Disease. Cell 164, 603–615. 10.1016/j.cell.2015.12.056. [PubMed: 26871627]

de Wilde MC, Overk CR, Sijben JW, and Masliah E (2016). Meta-analysis of synaptic pathology in Alzheimer's disease reveals selective molecular vesicular machinery vulnerability. Alzheimers Dement 12, 633–644. 10.1016/j.jalz.2015.12.005. [PubMed: 26776762]

Del-Aguila JL, Li Z, Dube U, Mihindukulasuriya KA, Budde JP, Fernandez MV, Ibanez L, Bradley J, Wang F, Bergmann K, et al. (2019). A single-nuclei RNA sequencing study of Mendelian and sporadic AD in the human brain. Alzheimers Res Ther 11, 71. 10.1186/s13195-019-0524-x. [PubMed: 31399126]

Dunckley T, Beach TG, Ramsey KE, Grover A, Mastroeni D, Walker DG, LaFleur BJ, Coon KD, Brown KM, Caselli R, et al. (2006). Gene expression correlates of neurofibrillary tangles in Alzheimer's disease. Neurobiol Aging 27, 1359–1371. 10.1016/j.neurobiolaging.2005.08.013. [PubMed: 16242812]

Farris W, Schütz SG, Cirrito JR, Shankar GM, Sun X, George A, Leissring MA, Walsh DM, Qiu WQ, Holtzman DM, and Selkoe DJ (2007). Loss of neprilysin function promotes amyloid plaque formation and causes cerebral amyloid angiopathy. Am J Pathol 171, 241–251. 10.2353/ajpath.2007.070105. [PubMed: 17591969]

Finak G, McDavid A, Yajima M, Deng J, Gersuk V, Shalek AK, Slichter CK, Miller HW, McElrath MJ, Prlic M, et al. (2015). MAST: a flexible statistical framework for assessing transcriptional changes and characterizing heterogeneity in single-cell RNA sequencing data. Genome Biol 16, 278. 10.1186/s13059-015-0844-5. [PubMed: 26653891]

Franzmeier N, Rubinski A, Neitzel J, Kim Y, Damm A, Na DL, Kim HJ, Lyoo CH, Cho H, Finsterwalder S, et al. (2019). Functional connectivity associated with tau levels in ageing, Alzheimer's, and small vessel disease. Brain 142, 1093–1107. 10.1093/brain/awz026. [PubMed: 30770704]

Frisoni GB, Fox NC, Jack CR, Scheltens P, and Thompson PM (2010). The clinical use of structural MRI in Alzheimer disease. Nat Rev Neurol 6, 67–77. 10.1038/nrneurol.2009.215. [PubMed: 20139996]

Frith MC, Fu Y, Yu L, Chen JF, Hansen U, and Weng Z (2004). Detection of functional DNA motifs via statistical over-representation. Nucleic Acids Res 32, 1372–1381. 10.1093/nar/gkh299. [PubMed: 14988425]

Frost B, Hemberg M, Lewis J, and Feany MB (2014). Tau promotes neurodegeneration through global chromatin relaxation. Nat Neurosci 17, 357–366. 10.1038/nn.3639. [PubMed: 24464041]

Fu AK, Hung KW, Huang H, Gu S, Shen Y, Cheng EY, Ip FC, Huang X, Fu WY, and Ip NY (2014). Blockade of EphA4 signaling ameliorates hippocampal synaptic dysfunctions in mouse models of Alzheimer's disease. Proc Natl Acad Sci U S A 111, 9959–9964. 10.1073/pnas.1405803111. [PubMed: 24958880]

Fu H, Hardy J, and Duff KE (2018). Selective vulnerability in neurodegenerative diseases. Nat Neurosci. 10.1038/s41593-018-0221-2.

Fu H, Possenti A, Freer R, Nakano Y, Villegas NCH, Tang M, Cauhy PVM, Lassus BA, Chen S, Fowler SL, et al. (2019). A tau homeostasis signature is linked with the cellular and regional vulnerability of excitatory neurons to tau pathology. Nat Neurosci 22, 47–56. 10.1038/s41593-018-0298-7. [PubMed: 30559469]

Gibbons GS, Lee VMY, and Trojanowski JQ (2019). Mechanisms of Cell-to-Cell Transmission of Pathological Tau: A Review. JAMA Neurol 76, 101–108. 10.1001/jamaneurol.2018.2505. [PubMed: 30193298]

Gómez-Isla T, Price JL, McKeel DW, Morris JC, Growdon JH, and Hyman BT (1996). Profound loss of layer II entorhinal cortex neurons occurs in very mild Alzheimer's disease. J Neurosci 16, 4491–4500. [PubMed: 8699259]

Greicius MD, Srivastava G, Reiss AL, and Menon V (2004). Default-mode network activity distinguishes Alzheimer's disease from healthy aging: evidence from functional MRI. Proc Natl Acad Sci U S A 101, 4637–4642. 10.1073/pnas.0308627101. [PubMed: 15070770]

Grindberg RV, Yee-Greenbaum JL, McConnell MJ, Novotny M, O'Shaughnessy AL, Lambert GM, Araúzo-Bravo MJ, Lee J, Fishman M, Robbins GE, et al. (2013). RNA-sequencing from single nuclei. Proc Natl Acad Sci U S A 110, 19802–19807. 10.1073/pnas.1319700110. [PubMed: 24248345]

Grubman A, Chew G, Ouyang JF, Sun G, Choo XY, McLean C, Simmons RK, Buckberry S, Vargas-Landin DB, Poppe D, et al. (2019). A single-cell atlas of entorhinal cortex from individuals with Alzheimer's disease reveals cell-type-specific gene expression regulation. Nat Neurosci 22, 2087–2097. 10.1038/s41593-019-0539-4. [PubMed: 31768052]

Habib N, Avraham-Davidi I, Basu A, Burks T, Shekhar K, Hofree M, Choudhury SR, Aguet F, Gelfand E, Ardlie K, et al. (2017). Massively parallel single-nucleus RNA-seq with DroNc-seq. Nat Methods. 10.1038/nmeth.4407.

Hafemeister C, and Satija R (2019). Normalization and variance stabilization of single-cell RNA-seq data using regularized negative binomial regression. Genome Biol 20, 296. 10.1186/s13059-019-1874-1. [PubMed: 31870423]

Hanseeuw BJ, Betensky RA, Jacobs HIL, Schultz AP, Sepulcre J, Becker JA, Cosio DMO, Farrell M, Quiroz YT, Mormino EC, et al. (2019). Association of Amyloid and Tau With Cognition in Preclinical Alzheimer Disease: A Longitudinal Study. JAMA Neurol. 10.1001/jamaneurol.2019.1424.

Hardy J, and Selkoe DJ (2002). The amyloid hypothesis of Alzheimer's disease: progress and problems on the road to therapeutics. Science 297, 353–356. 10.1126/science.1072994. [PubMed: 12130773]

Harris JA, Mihalas S, Hirokawa KE, Whitesell JD, Choi H, Bernard A, Bohn P, Caldejon S, Casal L, Cho A, et al. (2019). Hierarchical organization of cortical and thalamic connectivity. Nature 575, 195–202. 10.1038/s41586-019-1716-z. [PubMed: 31666704]

Harris KD, and Shepherd GM (2015). The neocortical circuit: themes and variations. Nat Neurosci 18, 170–181. 10.1038/nn.3917. [PubMed: 25622573]

Hodge RD, Bakken TE, Miller JA, Smith KA, Barkan ER, Graybuck LT, Close JL, Long B, Johansen N, Penn O, et al. (2019). Conserved cell types with divergent features in human versus mouse cortex. Nature. 10.1038/s41586-019-1506-7.

Hoerder-Suabedissen A, Hayashi S, Upton L, Nolan Z, Casas-Torremocha D, Grant E, Viswanathan S, Kanold PO, Clasca F, Kim Y, and Molnár Z (2018). Subset of Cortical Layer 6b Neurons Selectively Innervates Higher Order Thalamic Nuclei in Mice. Cereb Cortex 28, 1882–1897. 10.1093/cercor/bhy036. [PubMed: 29481606]

Hof PR, Cox K, and Morrison JH (1990). Quantitative analysis of a vulnerable subset of pyramidal neurons in Alzheimer's disease: I. Superior frontal and inferior temporal cortex. J Comp Neurol 301, 44–54. 10.1002/cne.903010105. [PubMed: 2127598]

Hof PR, Cox K, Young WG, Celio MR, Rogers J, and Morrison JH (1991). Parvalbumin-immunoreactive neurons in the neocortex are resistant to degeneration in Alzheimer's disease. J Neuropathol Exp Neurol 50, 451–462. [PubMed: 2061713]

Hof PR, Nimchinsky EA, Celio MR, Bouras C, and Morrison JH (1993). Calretinin-immunoreactive neocortical interneurons are unaffected in Alzheimer's disease. Neurosci Lett 152, 145–148. [PubMed: 8515868]

Hyman BT, Phelps CH, Beach TG, Bigio EH, Cairns NJ, Carrillo MC, Dickson DW, Duyckaerts C, Frosch MP, Masliah E, et al. (2012). National Institute on Aging-Alzheimer's Association guidelines for the neuropathologic assessment of Alzheimer's disease. Alzheimers Dement 8, 1–13. 10.1016/j.jalz.2011.10.007. [PubMed: 22265587]

Ittner A, Chua SW, Bertz J, Volkerling A, van der Hoven J, Gladbach A, Przybyla M, Bi M, van Hummel A, Stevens CH, et al. (2016). Site-specific phosphorylation of tau inhibits amyloid-β toxicity in Alzheimer's mice. Science 354, 904–908.10.1126/science.aah6205. [PubMed: 27856911]

Iwata N, Tsubuki S, Takaki Y, Shirotani K, Lu B, Gerard NP, Gerard C, Hama E, Lee HJ, and Saido TC (2001). Metabolic regulation of brain Abeta by neprilysin. Science 292, 1550–1552. 10.1126/science.1059946. [PubMed: 11375493]

Izzo NJ, Xu J, Zeng C, Kirk MJ, Mozzoni K, Silky C, Rehak C, Yurko R, Look G, Rishton G, et al. (2014). Alzheimer's therapeutics targeting amyloid beta 1-42 oligomers II: Sigma-2/PGRMC1 receptors mediate Abeta 42 oligomer binding and synaptotoxicity. PLoS One 9, e111899. 10.1371/journal.pone.0111899. [PubMed: 25390692]

Jack CR, Bennett DA, Blennow K, Carrillo MC, Dunn B, Haeberlein SB, Holtzman DM, Jagust W, Jessen F, Karlawish J, et al. (2018). NIA-AA Research Framework: Toward a biological definition of Alzheimer's disease. Alzheimers Dement 14, 535–562. 10.1016/j.jalz.2018.02.018. [PubMed: 29653606]

Jack CR, Knopman DS, Jagust WJ, Shaw LM, Aisen PS, Weiner MW, Petersen RC, and Trojanowski JQ (2010). Hypothetical model of dynamic biomarkers of the Alzheimer's pathological cascade. Lancet Neurol 9, 119–128. 10.1016/S1474-4422(09)70299-6. [PubMed: 20083042]

Kaeser PS, Deng L, Fan M, and Südhof TC (2012). RIM genes differentially contribute to organizing presynaptic release sites. Proc Natl Acad Sci U S A 109, 11830–11835. 10.1073/pnas.1209318109. [PubMed: 22753485]

Klein HU, McCabe C, Gjoneska E, Sullivan SE, Kaskow BJ, Tang A, Smith RV, Xu J, Pfenning AR, Bernstein BE, et al. (2019). Epigenome-wide study uncovers large-scale changes in histone acetylation driven by tau pathology in aging and Alzheimer's human brains. Nat Neurosci 22, 37–46. 10.1038/s41593-018-0291-1. [PubMed: 30559478]

Koopmans F, van Nierop P, Andres-Alonso M, Byrnes A, Cijsouw T, Coba MP, Cornelisse LN, Farrell RJ, Goldschmidt HL, Howrigan DP, et al. (2019). SynGO: An Evidence-Based, Expert-Curated Knowledge Base for the Synapse. Neuron 103, 217–234.e214. 10.1016/j.neuron.2019.05.002. [PubMed: 31171447]

Krishnaswami SR, Grindberg RV, Novotny M, Venepally P, Lacar B, Bhutani K, Linker SB, Pham S, Erwin JA, Miller JA, et al. (2016). Using single nuclei for RNA-seq to capture the transcriptome of postmortem neurons. Nat Protoc 11, 499–524. 10.1038/nprot.2016.015. [PubMed: 26890679]

Kuchibhotla KV, Wegmann S, Kopeikina KJ, Hawkes J, Rudinskiy N, Andermann ML, Spires-Jones TL, Bacskai BJ, and Hyman BT (2014). Neurofibrillary tangle-bearing neurons are functionally integrated in cortical circuits in vivo. Proc Natl Acad Sci U S A 111, 510–514. 10.1073/pnas.1318807111. [PubMed: 24368848]

Kunkle BW, Grenier-Boley B, Sims R, Bis JC, Damotte V, Naj AC, Boland A, Vronskaya M, van der Lee SJ, Amlie-Wolf A, et al. (2019). Genetic meta-analysis of diagnosed Alzheimer's disease identifies new risk loci and implicates Aβ, tau, immunity and lipid processing. Nat Genet 51, 414–430. 10.1038/s41588-019-0358-2. [PubMed: 30820047]

Lake BB, Ai R, Kaeser GE, Salathia NS, Yung YC, Liu R, Wildberg A, Gao D, Fung HL, Chen S, et al. (2016). Neuronal subtypes and diversity revealed by single-nucleus RNA sequencing of the human brain. Science 352, 1586–1590. 10.1126/science.aaf1204. [PubMed: 27339989]

Lake BB, Codeluppi S, Yung YC, Gao D, Chun J, Kharchenko PV, Linnarsson S, and Zhang K (2017). A comparative strategy for single-nucleus and single-cell transcriptomes confirms accuracy in predicted cell-type expression from nuclear RNA. Sci Rep 7, 6031. 10.1038/s41598-017-04426-w. [PubMed: 28729663]

Laurén J, Gimbel DA, Nygaard HB, Gilbert JW, and Strittmatter SM (2009). Cellular prion protein mediates impairment of synaptic plasticity by amyloid-beta oligomers. Nature 457, 1128–1132. 10.1038/nature07761. [PubMed: 19242475]

Leng K, Li E, Eser R, Piergies A, Sit R, Tan M, Neff N, Li SH, Rodriguez RD, Suemoto CK, et al. (2021). Molecular characterization of selectively vulnerable neurons in Alzheimer's disease. Nat Neurosci 24, 276–287. 10.1038/s41593-020-00764-7. [PubMed: 33432193]

Lewis J, and Dickson DW (2016). Propagation of tau pathology: hypotheses, discoveries, and yet unresolved questions from experimental and human brain studies. Acta Neuropathol 131, 27–48. 10.1007/s00401-015-1507-z. [PubMed: 26576562]

Lu T, Aron L, Zullo J, Pan Y, Kim H, Chen Y, Yang TH, Kim HM, Drake D, Liu XS, et al. (2014). REST and stress resistance in ageing and Alzheimer's disease. Nature 507, 448–454. 10.1038/nature13163. [PubMed: 24670762]

Malpetti M, Kievit RA, Passamonti L, Jones PS, Tsvetanov KA, Rittman T, Mak E, Nicastro N, Bevan-Jones WR, Su L, et al. (2020). Microglial activation and tau burden predict cognitive decline in Alzheimer's disease. Brain 143, 1588–1602. 10.1093/brain/awaa088. [PubMed: 32380523]

Mathys H, Davila-Velderrain J, Peng Z, Gao F, Mohammadi S, Young JZ, Menon M, He L, Abdurrob F, Jiang X, et al. (2019). Single-cell transcriptomic analysis of Alzheimer's disease. Nature 570, 332–337. 10.1038/s41586-019-1195-2. [PubMed: 31042697]

Mattsson N, Andreasson U, Zetterberg H, Blennow K, and Initiative A.s.D.N. (2017). Association of Plasma Neurofilament Light With Neurodegeneration in Patients With Alzheimer Disease. JAMA Neurol 74, 557–566. 10.1001/jamaneurol.2016.6117. [PubMed: 28346578]

Matys V, Fricke E, Geffers R, Gössling E, Haubrock M, Hehl R, Hornischer K, Karas D, Kel AE, Kel-Margoulis OV, et al. (2003). TRANSFAC: transcriptional regulation, from patterns to profiles. Nucleic Acids Res 31, 374–378. 10.1093/nar/gkg108. [PubMed: 12520026]

Menkes-Caspi N, Yamin HG, Kellner V, Spires-Jones TL, Cohen D, and Stern EA (2015). Pathological tau disrupts ongoing network activity. Neuron 85, 959–966. 10.1016/j.neuron.2015.01.025. [PubMed: 25704951]

Merico D, Isserlin R, Stueker O, Emili A, and Bader GD (2010). Enrichment map: a network-based method for gene-set enrichment visualization and interpretation. PLoS One 5, e13984. 10.1371/journal.pone.0013984. [PubMed: 21085593]

Merlini M, Rafalski VA, Ma K, Kim KY, Bushong EA, Rios Coronado PE, Yan Z, Mendiola AS, Sozmen EG, Ryu JK, et al. (2021). Microglial G i -dependent dynamics regulate brain network hyperexcitability. Nat Neurosci 24, 19–23. 10.1038/s41593-020-00756-7. [PubMed: 33318667]

Moloney CM, Lowe VJ, and Murray ME (2021). Visualization of neurofibrillary tangle maturity in Alzheimer's disease: A clinicopathologic perspective for biomarker research. Alzheimers Dement. 10.1002/alz.12321.

Moore S, Evans LD, Andersson T, Portelius E, Smith J, Dias TB, Saurat N, McGlade A, Kirwan P, Blennow K, et al. (2015). APP metabolism regulates tau proteostasis in human cerebral cortex neurons. Cell Rep 11, 689–696. 10.1016/j.celrep.2015.03.068. [PubMed: 25921538]

Morabito S, Miyoshi E, Michael N, and Swarup V (2020). Integrative genomics approach identifies conserved transcriptomic networks in Alzheimer's disease. Hum Mol Genet 29, 2899–2919. 10.1093/hmg/ddaa182. [PubMed: 32803238]

Mostafavi S, Gaiteri C, Sullivan SE, White CC, Tasaki S, Xu J, Taga M, Klein HU, Patrick E, Komashko V, et al. (2018). A molecular network of the aging human brain provides insights into the pathology and cognitive decline of Alzheimer's disease. Nat Neurosci 21, 811–819. 10.1038/s41593-018-0154-9. [PubMed: 29802388]

Nelson PT, Alafuzoff I, Bigio EH, Bouras C, Braak H, Cairns NJ, Castellani RJ, Crain BJ, Davies P, Del Tredici K, et al. (2012). Correlation of Alzheimer disease neuropathologic changes with cognitive status: a review of the literature. J Neuropathol Exp Neurol 71, 362–381. 10.1097/NEN.0b013e31825018f7. [PubMed: 22487856]

Ohnishi T, Yanazawa M, Sasahara T, Kitamura Y, Hiroaki H, Fukazawa Y, Kii I, Nishiyama T, Kakita A, Takeda H, et al. (2015). Na, K-ATPase α3 is a death target of Alzheimer patient amyloid-β assembly. Proc Natl Acad Sci U S A 112, E4465–4474. 10.1073/pnas.1421182112. [PubMed: 26224839]

Ossenkoppele R, Schonhaut DR, Schöll M, Lockhart SN, Ayakta N, Baker SL, O'Neil JP, Janabi M, Lazaris A, Cantwell A, et al. (2016). Tau PET patterns mirror clinical and neuroanatomical variability in Alzheimer's disease. Brain 139, 1551–1567. 10.1093/brain/aww027. [PubMed: 26962052]

Pakos-Zebrucka K, Koryga I, Mnich K, Ljujic M, Samali A, and Gorman AM (2016). The integrated stress response. EMBO Rep 17, 1374–1395. 10.15252/embr.201642195. [PubMed: 27629041]

Palop JJ, and Mucke L (2016). Network abnormalities and interneuron dysfunction in Alzheimer disease. Nat Rev Neurosci 17, 777–792. 10.1038/nrn.2016.141. [PubMed: 27829687]

Parikshak NN, Swarup V, Belgard TG, Irimia M, Ramaswami G, Gandal MJ, Hartl C, Leppa V, Ubieta LT, Huang J, et al. (2016). Genome-wide changes in lncRNA, splicing, and regional gene expression patterns in autism. Nature 540, 423–427. 10.1038/nature20612. [PubMed: 27919067]

Pickett EK, Herrmann AG, McQueen J, Abt K, Dando O, Tulloch J, Jain P, Dunnett S, Sohrabi S, Fjeldstad MP, et al. (2019). Amyloid Beta and Tau Cooperate to Cause Reversible Behavioral and Transcriptional Deficits in a Model of Alzheimer's Disease. Cell Rep 29, 3592–3604.e3595. 10.1016/j.celrep.2019.11.044. [PubMed: 31825838]

Piras A, Collin L, Grüninger F, Graff C, and Rönnbäck A (2016). Autophagic and lysosomal defects in human tauopathies: analysis of post-mortem brain from patients with familial Alzheimer disease, corticobasal degeneration and progressive supranuclear palsy. Acta Neuropathol Commun 4, 22. 10.1186/s40478-016-0292-9. [PubMed: 26936765]

Plaisier SB, Taschereau R, Wong JA, and Graeber TG (2010). Rank-rank hypergeometric overlap: identification of statistically significant overlap between gene-expression signatures. Nucleic Acids Res 38, e169. 10.1093/nar/gkq636. [PubMed: 20660011]

Puzzo D, Argyrousi EK, Staniszewski A, Zhang H, Calcagno E, Zuccarello E, Acquarone E, Fa' M, Li Puma DD, Grassi C, et al. (2020). Tau is not necessary for amyloid-β-induced synaptic and memory impairments. J Clin Invest 130, 4831–4844. 10.1172/JCI137040. [PubMed: 32544084]

Puzzo D, Piacentini R, Fá M, Gulisano W, Li Puma DD, Staniszewski A, Zhang H, Tropea MR, Cocco S, Palmeri A, et al. (2017). LTP and memory impairment caused by extracellular Aβ and Tau oligomers is APP-dependent. Elife 6. 10.7554/eLife.26991.

Raichle ME, MacLeod AM, Snyder AZ, Powers WJ, Gusnard DA, and Shulman GL (2001). A default mode of brain function. Proc Natl Acad Sci U S A 98, 676–682. 10.1073/pnas.98.2.676. [PubMed: 11209064]

Raudvere U, Kolberg L, Kuzmin I, Arak T, Adler P, Peterson H, and Vilo J (2019). g:Profiler: a web server for functional enrichment analysis and conversions of gene lists (2019 update). Nucleic Acids Res 47, W191–W198. 10.1093/nar/gkz369. [PubMed: 31066453]

Reimand J, Isserlin R, Voisin V, Kucera M, Tannus-Lopes C, Rostamianfar A, Wadi L, Meyer M, Wong J, Xu C, et al. (2019). Pathway enrichment analysis and visualization of omics data using g:Profiler, GSEA, Cytoscape and EnrichmentMap. Nat Protoc 14, 482–517. 10.1038/s41596-018-0103-9. [PubMed: 30664679]

Rossier J, Bernard A, Cabungcal JH, Perrenoud Q, Savoye A, Gallopin T, Hawrylycz M, Cuénod M, Do K, Urban A, and Lein ES (2015). Cortical fast-spiking parvalbumin interneurons enwrapped in the perineuronal net express the metallopeptidases Adamts8, Adamts15 and Neprilysin. Mol Psychiatry 20, 154–161. 10.1038/mp.2014.162. [PubMed: 25510509]

Roussarie JP, Yao V, Rodriguez-Rodriguez P, Oughtred R, Rust J, Plautz Z, Kasturia S, Albornoz C, Wang W, Schmidt EF, et al. (2020). Selective Neuronal Vulnerability in Alzheimer's Disease: A Network-Based Analysis. Neuron 107, 821–835.e812. 10.1016/j.neuron.2020.06.010. [PubMed: 32603655]

Rovelet-Lecrux A, Hannequin D, Raux G, Le Meur N, Laquerrière A, Vital A, Dumanchin C, Feuillette S, Brice A, Vercelletto M, et al. (2006). APP locus duplication causes autosomal dominant early-onset Alzheimer disease with cerebral amyloid angiopathy. Nat Genet 38, 24–26. 10.1038/ngl718. [PubMed: 16369530]

Rüb U, Stratmann K, Heinsen H, Del Turco D, Ghebremedhin E, Seidel K, den Dunnen W, and Korf HW (2016). Hierarchical Distribution of the Tau Cytoskeletal Pathology in the Thalamus of Alzheimer's Disease Patients. J Alzheimers Dis 49, 905–915. 10.3233/JAD-150639. [PubMed: 26519431]

Saiz-Sanchez D, De la Rosa-Prieto C, Ubeda-Banon I, and Martinez-Marcos A (2015). Interneurons, tau and amyloid-β in the piriform cortex in Alzheimer's disease. Brain Struct Funct 220, 2011–2025. 10.1007/s00429-014-0771-3. [PubMed: 24748561]

Schöll M, Lockhart SN, Schonhaut DR, O'Neil JP, Janabi M, Ossenkoppele R, Baker SL, Vogel JW, Faria J, Schwimmer HD, et al. (2016). PET Imaging of Tau Deposition in the Aging Human Brain. Neuron 89, 971–982. 10.1016/j.neuron.2016.01.028. [PubMed: 26938442]

Schwarz AJ, Yu P, Miller BB, Shcherbinin S, Dickson J, Navitsky M, Joshi AD, Devous MD, and Mintun MS (2016). Regional profiles of the candidate tau PET ligand 18F-AV-1451 recapitulate key features of Braak histopathological stages. Brain 139, 1539–1550. 10.1093/brain/aww023. [PubMed: 26936940]

Seeley WW, Crawford RK, Zhou J, Miller BL, and Greicius MD (2009). Neurodegenerative diseases target large-scale human brain networks. Neuron 62, 42–52. 10.1016/j.neuron.2009.03.024. [PubMed: 19376066]

Serrano-Pozo A, Frosch MP, Masliah E, and Hyman BT (2011). Neuropathological alterations in Alzheimer disease. Cold Spring Harb Perspect Med 1, a006189. 10.1101/cshperspect.a006189. [PubMed: 22229116]

Shankar GM, Bloodgood BL, Townsend M, Walsh DM, Selkoe DJ, and Sabatini BL (2007). Natural oligomers of the Alzheimer amyloid-beta protein induce reversible synapse loss by modulating an NMDA-type glutamate receptor-dependent signaling pathway. J Neurosci 27, 2866–2875. 10.1523/JNEUROSCI.4970-06.2007. [PubMed: 17360908]

Shen Y, Ge WP, Li Y, Hirano A, Lee HY, Rohlmann A, Missler M, Tsien RW, Jan LY, Fu YH, and Ptáček LJ (2015). Protein mutated in paroxysmal dyskinesia interacts with the active zone protein RIM and suppresses synaptic vesicle exocytosis. Proc Natl Acad Sci U S A 112, 2935–2941. 10.1073/pnas.1501364112. [PubMed: 25730884]

Sherman MA, LaCroix M, Amar F, Larson ME, Forster C, Aguzzi A, Bennett DA, Ramsden M, and Lesné SE (2016). Soluble Conformers of Aβ and Tau Alter Selective Proteins Governing Axonal Transport. J Neurosci 36, 9647–9658. 10.1523/JNEUROSCI.1899-16.2016. [PubMed: 27629715]

Sierksma A, Lu A, Mancuso R, Fattorelli N, Thrupp N, Salta E, Zoco J, Blum D, Buée L, De Strooper B, and Fiers M (2020). Novel Alzheimer risk genes determine the microglia response to amyloid-β but not to TAU pathology. EMBO Mol Med 12, e10606. 10.15252/emmm.201910606. [PubMed: 31951107]

Soneson C, and Robinson MD (2018). Bias, robustness and scalability in single-cell differential expression analysis. Nat Methods 15, 255–261. 10.1038/nmeth.4612. [PubMed: 29481549]

Spires-Jones TL, de Calignon A, Matsui T, Zehr C, Pitstick R, Wu HY, Osetek JD, Jones PB, Bacskai BJ, Feany MB, et al. (2008). In vivo imaging reveals dissociation between caspase activation and acute neuronal death in tangle-bearing neurons. J Neurosci 28, 862–867. 10.1523/JNEUROSCI.3072-08.2008. [PubMed: 18216194]

Sun Y, Ip P, and Chakrabartty A (2017). Simple Elimination of Background Fluorescence in Formalin-Fixed Human Brain Tissue for Immunofluorescence Microscopy. J Vis Exp. 10.3791/56188.

Tagliafierro L, Bonawitz K, Glenn OC, and Chiba-Falek O (2016). Gene Expression Analysis of Neurons and Astrocytes Isolated by Laser Capture Microdissection from Frozen Human Brain Tissues. Front Mol Neurosci 9, 72. 10.3389/fnmol.2016.00072. [PubMed: 27587997]

Terry RD, Masliah E, Salmon DP, Butters N, DeTeresa R, Hill R, Hansen LA, and Katzman R (1991). Physical basis of cognitive alterations in Alzheimer's disease: synapse loss is the major correlate of cognitive impairment. Ann Neurol 30, 572–580. 10.1002/ana.410300410. [PubMed: 1789684]

Vogel JW, Iturria-Medina Y, Strandberg OT, Smith R, Levitis E, Evans AC, Hansson O, Initiative A.s.D.N., and Study SB (2020). Spread of pathological tau proteins through communicating neurons in human Alzheimer's disease. Nat Commun 11, 2612. 10.1038/s41467-020-15701-2. [PubMed: 32457389]

Wan YW, Al-Ouran R, Mangleburg CG, Perumal TM, Lee TV, Allison K, Swarup V, Funk CC, Gaiteri C, Allen M, et al. (2020). Meta-Analysis of the Alzheimer's Disease Human Brain Transcriptome and Functional Dissection in Mouse Models. Cell Rep 32, 107908. 10.1016/j.celrep.2020.107908. [PubMed: 32668255]

Wang Y, and Mandelkow E (2016). Tau in physiology and pathology. Nat Rev Neurosci 17, 5–21. 10.1038/nrn.2015.1. [PubMed: 26631930]

Wesseling H, Mair W, Kumar M, Schlaffner CN, Tang S, Beerepoot P, Fatou B, Guise AJ, Cheng L, Takeda S, et al. (2020). Tau PTM Profiles Identify Patient Heterogeneity and Stages of Alzheimer's Disease. Cell 183, 1699–1713.e1613. 10.1016/j.cell.2020.10.029. [PubMed: 33188775]

Yang ZF, Drumea K, Mott S, Wang J, and Rosmarin AG (2014). GABP transcription factor (nuclear respiratory factor 2) is required for mitochondrial biogenesis. Mol Cell Biol 34, 3194–3201. 10.1128/MCB.00492-12. [PubMed: 24958105]

Zeng H, Shen EH, Hohmann JG, Oh SW, Bernard A, Royall JJ, Glattfelder KJ, Sunkin SM, Morris JA, Guillozet-Bongaarts AL, et al. (2012). Large-scale cellular-resolution gene profiling in human neocortex reveals species-specific molecular signatures. Cell 149, 483–496. 10.1016/j.cell.2012.02.052. [PubMed: 22500809]

Zhou L, McInnes J, Wierda K, Holt M, Herrmann AG, Jackson RJ, Wang YC, Swerts J, Beyens J, Miskiewicz K, et al. (2017). Tau association with synaptic vesicles causes presynaptic dysfunction. Nat Commun 8, 15295. 10.1038/ncomms15295. [PubMed: 28492240]

Zott B, Simon MM, Hong W, Unger F, Chen-Engerer HJ, Frosch MP, Sakmann B, Walsh DM, and Konnerth A (2019). A vicious cycle of β amyloid-dependent neuronal hyperactivation. Science 365, 559–565. 10.1126/science.aay0198. [PubMed: 31395777]

Zullo JM, Drake D, Aron L, O'Hern P, Dhamne SC, Davidsohn N, Mao CA, Klein WH, Rotenberg A, Bennett DA, et al. (2019). Regulation of lifespan by neural excitation and REST. Nature 574, 359–364. 10.1038/s41586-019-1647-8. [PubMed: 31619788]

Highlights

- Method for profiling cells with cytoplasmic protein aggregates from the human brain
- Comparison of ~120K NFT-bearing and NFT-free transcriptomes from AD and controls
- Ranked list of 227 synaptic genes associated with NFTs in human prefrontal cortex
- Uncoupling of susceptibility to NFT formation and neuronal death

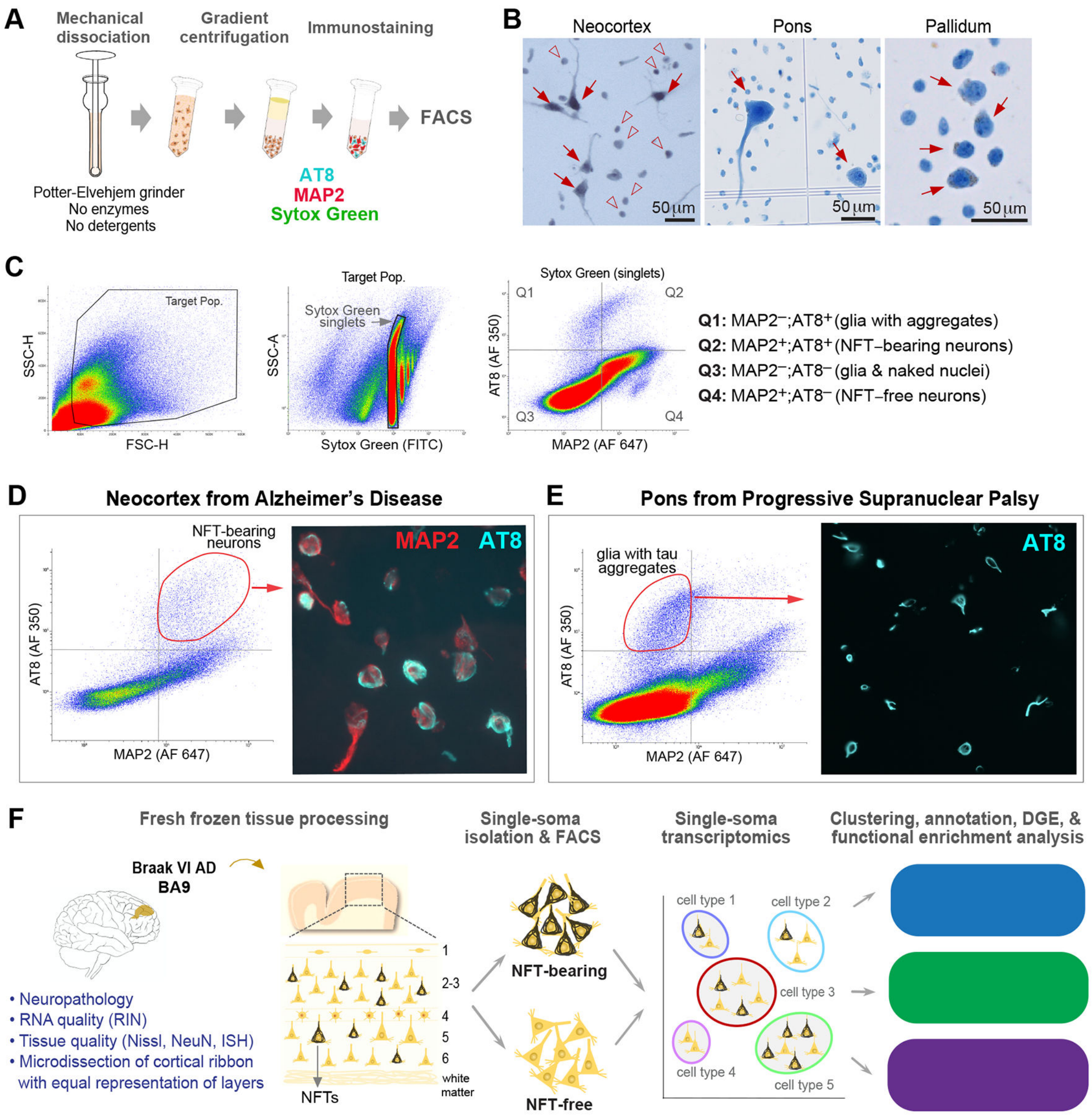

Figure 1. Isolation of single somas with pathological tau aggregates

(A) Experimental approach to single-soma isolation.

(B) Representative single cell suspensions displaying neuronal somas (arrows) and naked nuclei (arrowheads).

(C) Representative FACS plots of pallidum-derived somas from a PSP donor. Gating using MAP2 and AT8 allows the collection of glial cells with tau aggregates (Q1; MAP2^{-}/AT8^{+}), neuronal somas with tau aggregates (Q2; MAP2^{+}/AT8^{+}), and neuronal somas without aggregates (Q4; MAP2^{+}/AT8^{-}).

(D) FACS plot and sorted AT8^{+}/MAP2^{+} neurons displaying mature tangles (band or flamed shaped; arrowheads) and early perikaryal fibrils (arrow) from AD neocortex.

(E) FACS plot and sorted MAP2^{-}/AT8^{+} glia displaying oligodendrocytes with coiled bodies from a PSP donor.

(F) Overview of strategy for single-soma transcriptomics of NFT-bearing and NFT-free neurons from AD brain.

See also Figures S1 and S2.

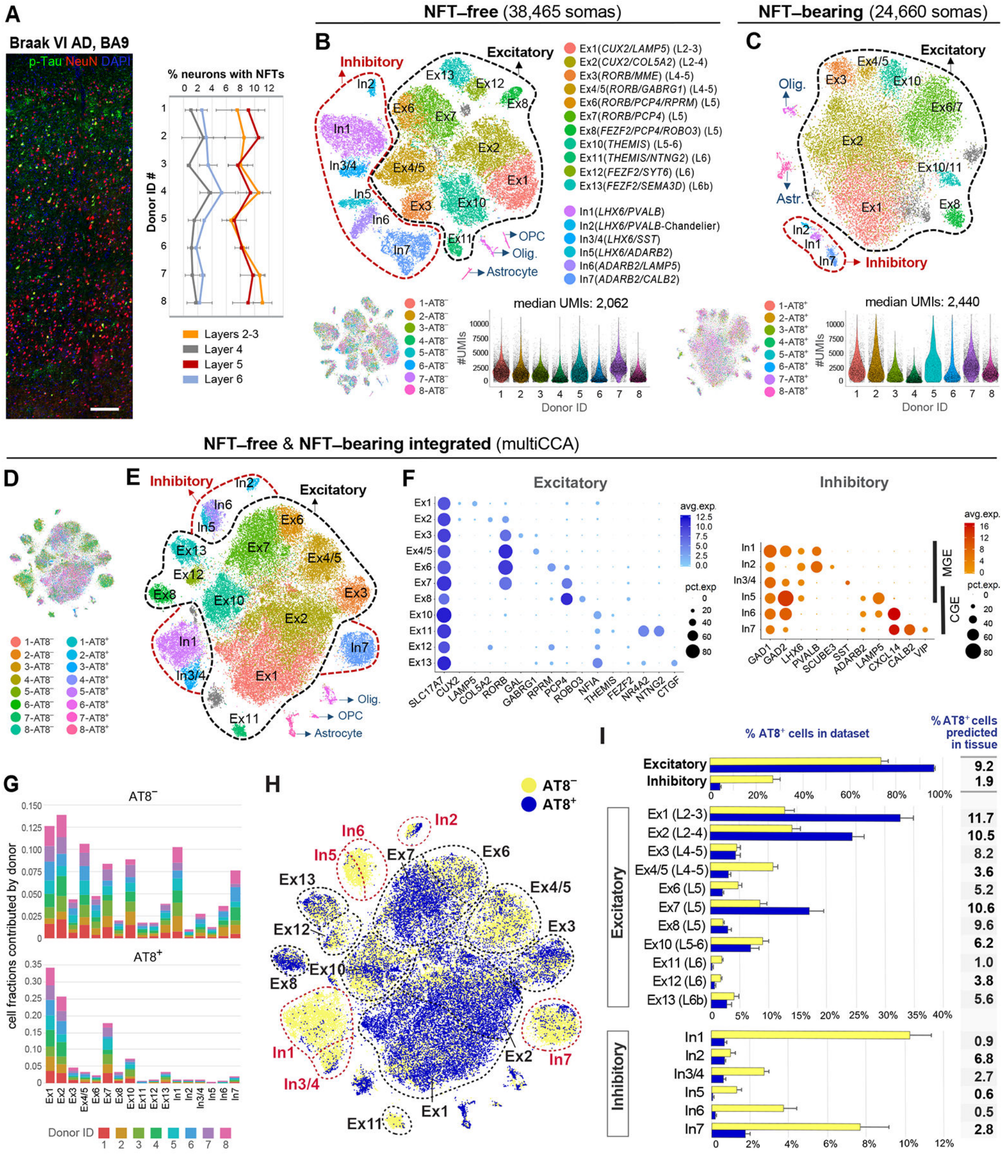

Figure 2. Census of neuronal subtypes exhibiting NFTs in AD

(A) Quantification of NFT density in tissues used for transcriptomics. NFTs were abundant in layers 2–3 (8.94 ± 1.52%) and 5 (8.86 ± 1.56%) and sparse in layers 4 (1.75 ± 1.03%) and 6 (3.03 ± 0.96%). Data are represented as mean ± STD.

(B and C) Clustering of NFT-free and NFT-bearing somas separately. t-SNE plots illustrate the annotated cell types. Gray clusters represent mixed populations. Violin plots show the distribution of UMI counts per cell in each sample.

(D–F) Clustering of NFT-free and NFT-bearing combined datasets after multiCCA (63,110 somas after QC). One color in (D) per sample. Unsupervised clustering (E) identified the same neuronal subtypes as in (B). Dot plots (F) depict the expression of marker genes (x-axis) within Ex and In clusters (y-axis).

(G) Bar plots illustrating the fraction of somas derived from each donor per cluster (normalized to sample size).

(H) t-SNE plot highlighting the relative contributions of $AT8^-$ and $AT8^+$ somas to each cluster.

(I) Bar plots showing the percentages of $AT8^-$ and $AT8^+$ somas per cluster. Data are represented as mean ± SEM. The column adjacent to the bar plots shows the predicted percentages of $AT8^+$ neurons in histological sections for each subtype (percentage of $AT8^+$ somas per cluster normalized to total somas obtained in clustering analysis divided by percentage of NFT-bearing neurons obtained in histological sections from the same donor [Figure 2A]).

See also Figures S3 and S4, and Table S2.

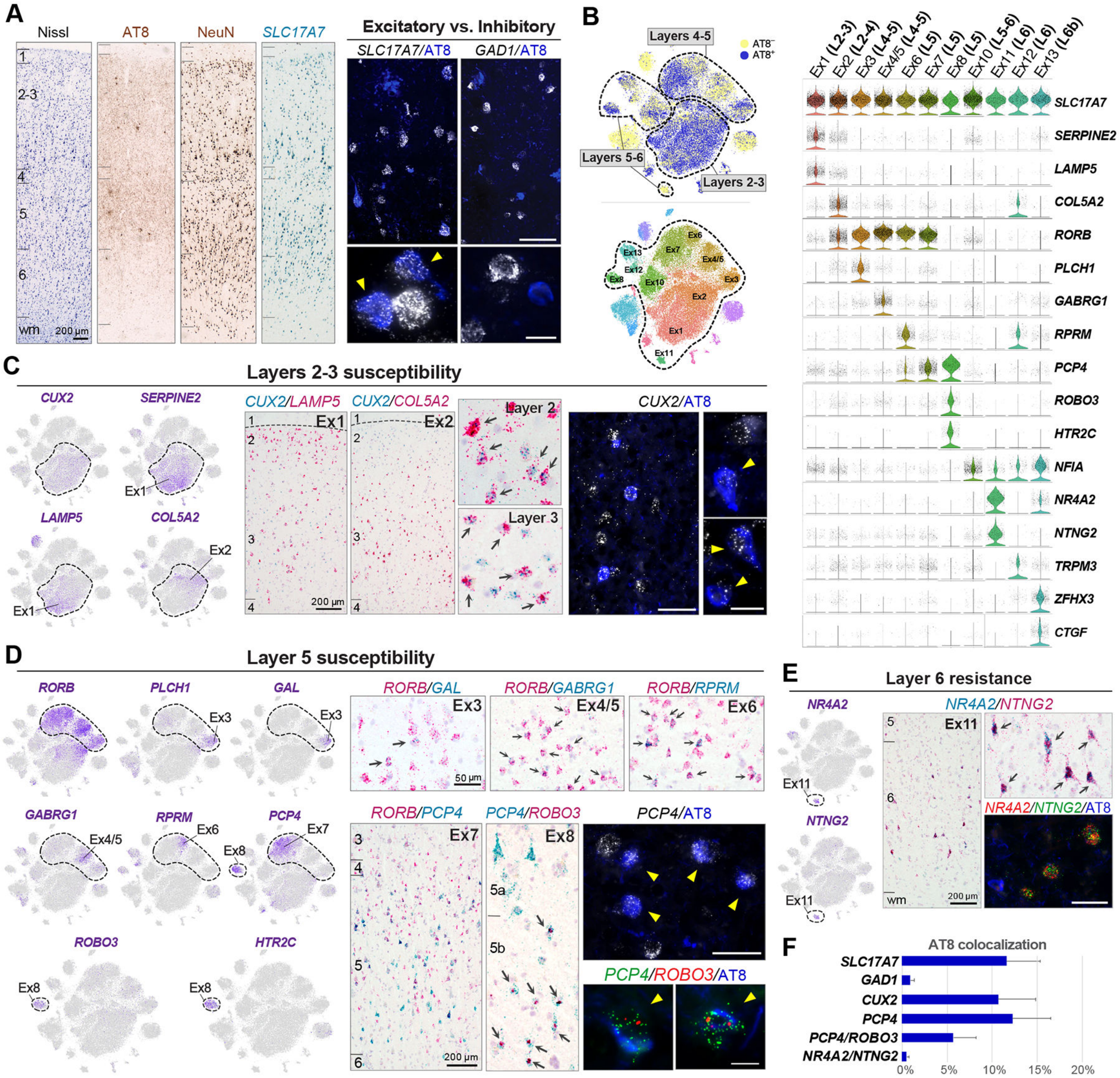

Figure 3. Histological validation of vulnerable excitatory neuronal subtypes

(A) Nissl, AT8 and NeuN IHC, and *SLC17A7* ISH provide anatomical reference. Double fluorescent AT8 IHC (blue) and ISH (white) stains illustrate susceptibility of excitatory (*SLC17A7*) and resistance of inhibitory (*GAD1*) neurons. Arrowheads point to neurons with NFTs.

(B) t-SNE and violin plots highlight marker genes for excitatory neuronal subtypes and their laminar distribution.

(C) Susceptibility of layers 2–3 *CUX2* (Ex1, Ex2) neurons. Feature plots illustrate gradient-like expression of *SERPINE2/LAMP5* and *COL5A2* within the *CUX2* cluster. Double chromogenic ISH illustrates two subpopulations with preferential distributions in superficial (*CUX2/LAMP5*$^+$; Ex1) or deep (*CUX2/COL5A2*$^+$; Ex2) layers 2–3. Arrows point to double-positive cells. Double fluorescent AT8 IHC and *CUX2* ISH illustrate *CUX2*$^+$ neurons with NFTs.

(D) Susceptibility of layer 5 *RORB/PCP4* (Ex7) and layer 5b *PCP4/ROBO3* (Ex8). Feature plots illustrate a heterogenous *RORB* population comprised of *RORB/PLCH1/GAL* (Ex3), *RORB/GABRG1* (Ex4/5), *RORB/RPRM* (Ex6), and *RORB/PCP4* (Ex7) clusters, and a *RORB*$^{-}$, *PCP4/ROBO3/HTR2C* cluster (Ex8). Double chromogenic ISH for *RORB* and either *GAL*, *GABRG1, RPRM* or *PCP4* confirmed distinct neuronal populations within layers 4–5. Double chromogenic ISH for *PCP4* and *ROBO3* illustrates small *PCP4/ROBO3*$^{+}$ neuronal bodies in layer 5b (arrows). Fluorescent staining for AT8 and either *PCP4* or *PCP4* and *ROBO3* illustrates neurons with NFTs.

(E) Resistance of layer 6 *NR4A2/NTNG2* (Ex11). Double chromogenic and triple fluorescent staining illustrate *AT8*$^{-}$, *NR4A2/NTNG2*$^{+}$ neurons.

(F) Bar plot showing the frequency of NFTs in cells expressing *SLC17A7* (11.59 ± 3.7%), *GAD1* (0.95 ± 0.41%), *CUX2* (10.64 ± 4.2%), *PCP4* (12.24 ± 4.2%), *PCP4/ROBO3* (5.70 ± 2.53%), and *NR4A2/NTNG2* (0.5 ± 0.3%). Error bars indicate STD.

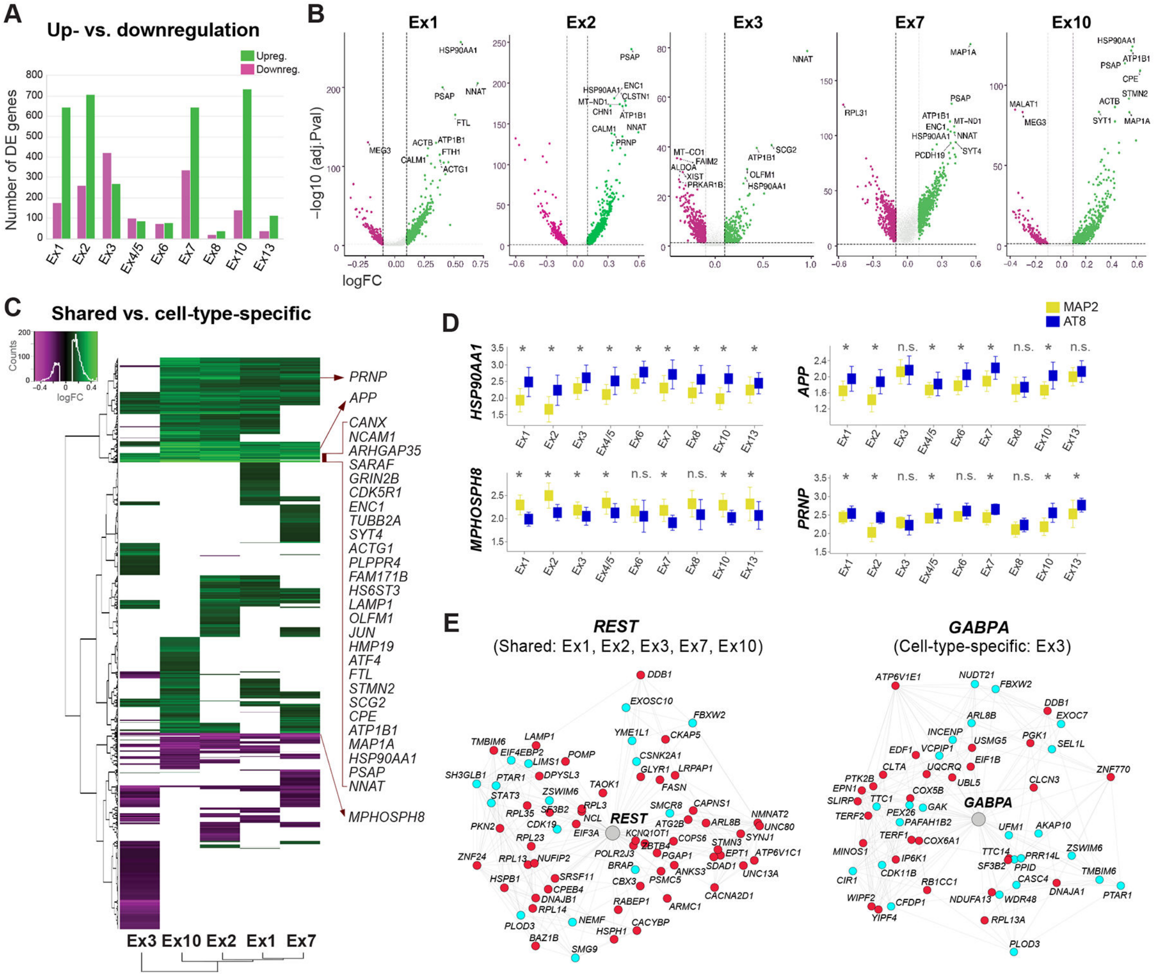

Figure 4. Transcriptomic signatures of tau pathology within and across neuronal subtypes

(A) Total numbers of up- and downregulated genes between neurons with and without NFTs.

(B) Volcano plots of DE genes for five excitatory subtypes with high NFT proportions. Dots represent genes (green = upregulated; magenta = downregulated). Dashed lines indicate significance thresholds (log-fold change <0.1 or > 0.1; adjusted p-value < 0.05; for genes detected in ≥ 20% of cells in at least one condition; MAST test). Top 10 DE genes are displayed.

(C) Heatmap and hierarchical clustering of DE genes highlighting shared and cell-type-specific up- and downregulated genes. Input lists of genes were truncated to match the cell type with the smallest number of DE genes. The genes listed include shared DE genes with the highest log-fold change values.

(D) Box plots showing median expression values of *HSP90AA1*, *APP*, *PRNP*, and the epigenetic repressor *MPHOSPH8* in neurons with and without NFTs in each cluster. *$p < 0.05$ (MAST test); n.s. = not significant.

(E) *REST* and *GABPA* transcriptional regulatory networks (color code: cyan = genes coregulated and coexpressed based on our single-cell data and/or ROSMAP datasets; red = genes coregulated, coexpressed, and differentially expressed in neurons with NFTs).

See also Figure S5 and Tables S2 and S3.

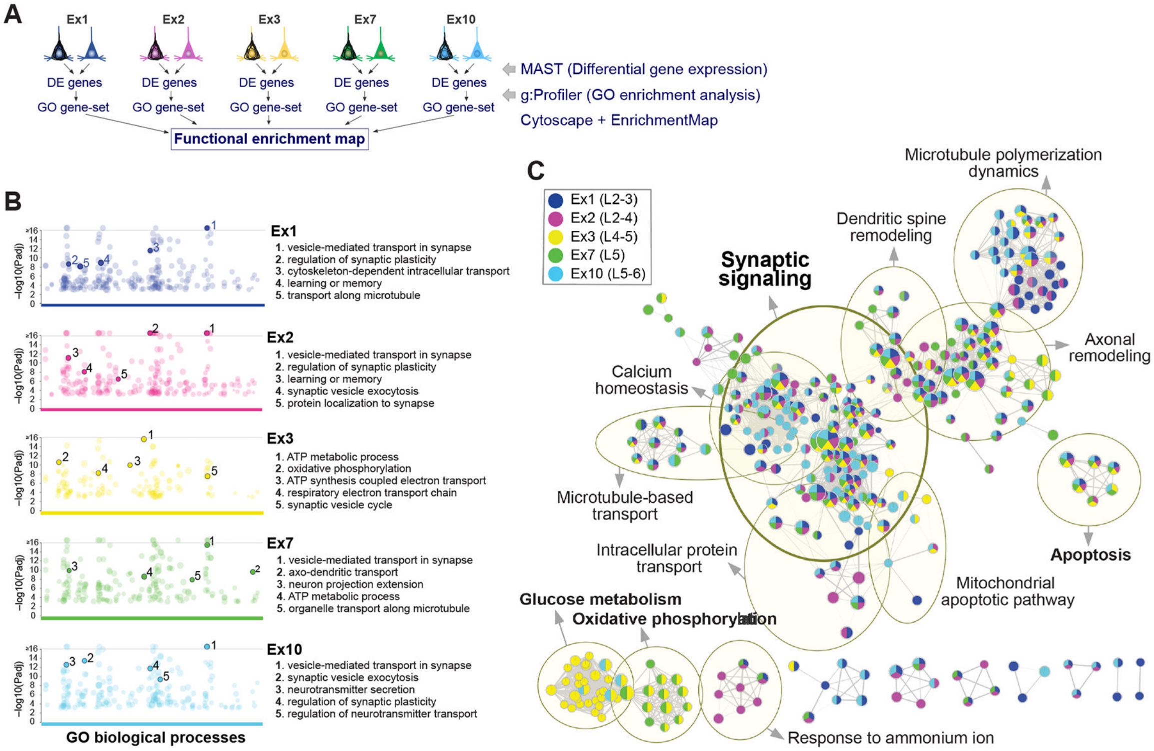

Figure 5. Shared versus cell-type-specific pathways associated with tau pathology

(A) Overview of strategy to identify shared and cell-type-specific pathways overrepresented in the five clusters with highest cell numbers and NFT proportions.

(B) Manhattan plots of GO biological processes enriched in NFT-bearing vs. NFT-free neurons for each cluster, obtained using g:Profiler. Colored circles represent significant terms (thresholds: g:SCS significance < 0.001; GO terms with > 50 or < 500 genes; capped at terms with a −log10 [Padj] > 16). Top 5 nonredundant terms are highlighted.

(C) Functional enrichment map. Nodes represent gene sets of GO biological processes; each node is color-coded by cluster to illustrate shared and cell-type-specific contributions. Yellow circles delineate constellations of functionally related gene sets.

See also Table S4.

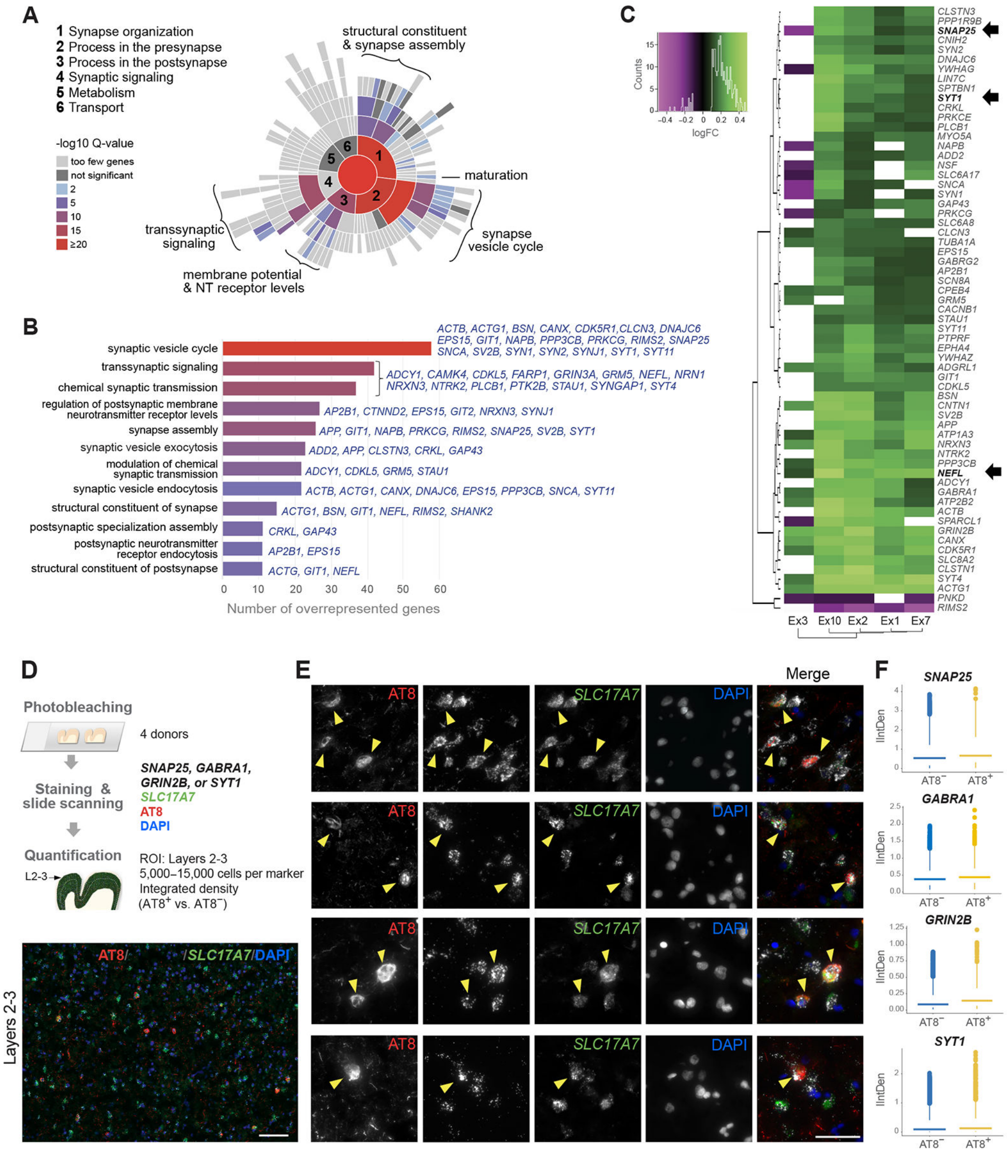

Figure 6. Dysregulation of synaptic transmission pathways in NFT-bearing neurons

(A and B) Enrichment of synaptic transmission pathways in NFT-bearing neurons by SynGO. Sunburst plot illustrates over- and underrepresented biological process terms; colors represent enrichment values at 1% FDR. The bar plot highlights top 12 enriched terms and commonly DE genes in NFT-bearing neurons within each term.

(C) Heatmap and hierarchical clustering of 63 synaptic genes dysregulated across five excitatory subtypes (green = upregulated; magenta = downregulated; MAST test with adjusted p-value < 0.05; log-fold change >0.1; detection in ≥ 20% of cells). Arrows indicate genes for known biomarkers.

(D) Experimental design to validate upregulation of synaptic markers in $AT8^+$ excitatory neurons. Representative section illustrates AT8 and *GRIN2B* colocalization in layers 2–3 *SLC17A7*$^+$ neurons (arrowheads).

(E) Representative double fluorescent ISH staining for *SLC17A7* and either *SNAP25*, *GABRA1*, *GRIN2B*, or *SYT1* in AT8$^+$ neurons (arrowheads).

(F) Quantification of integrated density (IntDen) of *SNAP25*, *GABRA1*, *GRIN2B*, or *SYT1* in AT8$^+$ vs. AT8$^-$ excitatory neurons. Average expression in AT8$^+$ vs. AT8$^-$ neurons for each donor was significantly increased for 3 of the 4 markers (paired t-test; n = 4 donors; p = 0.11 [*SNAP25*], p = 0.05 [*GABRA1*], p = 0.02 [*GRIN2B*], p = 0.04 [*SYT1*]). After fitting a linear mixed model to predict IntDen with AT8, using the donor as a random effect, the effect of AT8 was statistically significant and positive ($p < 0.001$) for all markers.

See also Figure S6 and Table S5.

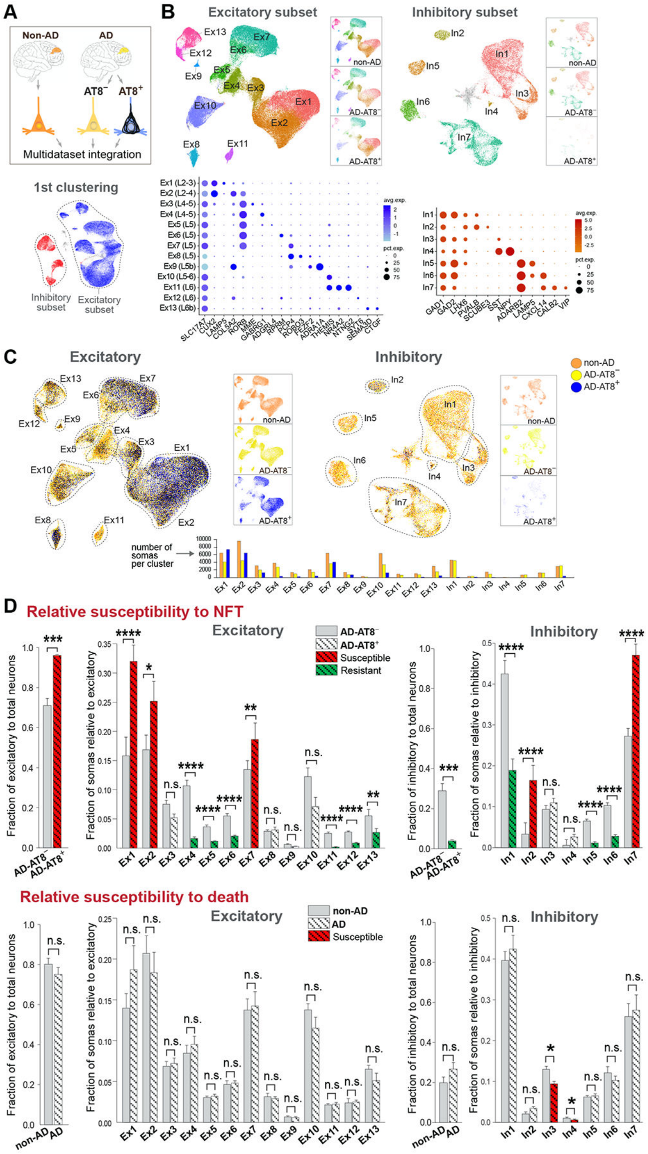

Figure 7. Uncoupling of NFT and neuronal death susceptibilities in AD

(A and B) Integration of non-AD, AD-AT8$^-$, and AD-AT8$^+$ datasets. UMAP plots show unsupervised clustering of excitatory and inhibitory subsets. The three datasets are split and represented side-by-side to illustrate similar cell compositions of the non-AD and AD-AT8$^-$ datasets, and different cell compositions of the AD-AT8$^+$ dataset. Dot plots (B) depict the expression of marker genes (x-axis) within Ex and In clusters (y-axis).

(C) UMAP plots highlighting relative contributions of non-AD, AD-AT8$^-$, and AD-AT8$^+$ somas to each Ex or In cluster.

(D) Bar plots showing fractions of AD-AT8$^+$ vs. AD-AT8$^-$ somas (relative susceptibility to exhibit NFTs) and fractions of non-AD vs. AD somas (interpreted as relative susceptibility to death). The red and green colors indicate the most susceptible and resistant subtypes (adjusted p-values: *p < 0.05, **p < 0.01, ***p < 0.001, and ****p < 0.0001; n.s. = not significant; beta regression analysis). Data are represented as mean ± SEM.

See also Figures S7 and S8 and Table S6.

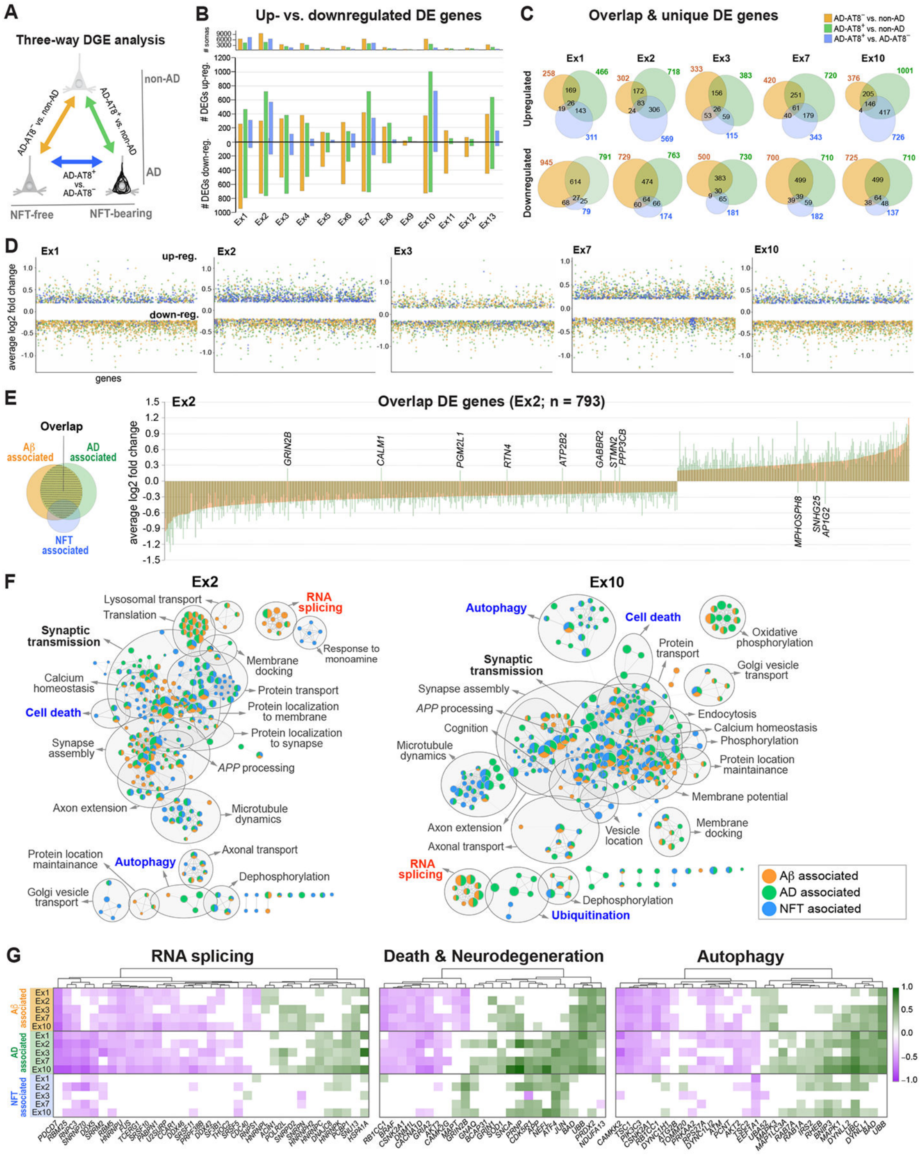

Figure 8. NFT-associated versus AD-associated transcriptomic changes in AD

(A) Three-way DGE analysis between non-AD, AD-AT8⁻, and AD-AT8⁺ datasets; colors represent DGE between each pair.

(B) Bar chart showing the total number of up- and downregulated genes for each comparison within each excitatory subtype.

(C) Venn diagrams showing the number of overlapping and unique DE genes for each comparison in five excitatory subtypes susceptible to tau aggregation.

(D) Scatter plots illustrating the distribution of up- and downregulated genes.

(E) Bar plot showing average log2 fold change values for overlap genes in a representative vulnerable subtype (Ex2). Each bar represents a DE gene (n = 793). The bars are overlaid (orange = AD-AT8⁻ vs. non-AD; green = AD-AT8⁺ vs. non-AD) to demonstrate the directionality and log2 fold change per gene for the two comparisons. Only the 11 genes named in the figure were dysregulated in opposite directions.

(F) Functional enrichment maps illustrating Aβ-associated, NFT-associated, and AD-associated terms. Nodes represent gene sets of GO biological processes. Gray circles delineate constellations of functionally related gene sets.

(G) Heatmaps of DE genes within the RNA splicing, death, and autophagy pathways highlighting Aβ-associated, NFT-associated, and AD-associated genes (green = upregulated; magenta = downregulated; MAST test with adjusted p-value < 0.05; log2 fold change >0.1; detection in ≥ 20% of cells).

See also Figure S9 and Table S7.

KEY RESOURCES TABLE

REAGENT or RESOURCE	**SOURCE**	**IDENTIFIER**
Antibodies		
Rabbit anti-MAP2 polyclonal	MilliporeSigma	Cat#AB5622
Mouse anti-NeuN	MilliporeSigma	Cat#MAB377
Mouse anti-phospho-Tau Ser202, Thr205 monoclonal (AT8)	ThermoFisher	Cat#MN1020
Rabbit polyclonal anti oligomeric tau (T22)	MilliporeSigma	Cat#ABN454
Recombinant rabbit anti-phospho-Tau (Ser396) monoclonal [EPR2731]	Abcam	Cat#ab109390
Phospho-Tau (Thr205) Polyclonal	ThermoFisher	Cat#44-738G
Recombinant anti-SQSTM1/p62 [EPR4844]	Abcam	Cat#ab109012
HRP Anti-beta Actin [AC-15]	Abcam	Cat# ab49900
Lamin B1 (D4Q4Z) Rabbit monoclonal	Cell Signaling Technology	Cat#12586
Histone H3 C-terminal	EpiCypher	Cat#13-0001
Biological Samples		
Human postmortem brain tissue	Table S1	N/A
Chemicals, Peptides, and Recombinant Proteins		
RNAscope Probe *SLC17A7*	ACD Bio	Cat#415611
RNAscope Probe *GAD1*	ACD Bio	Cat#404031
RNAscope Probe *CUX2*	ACD Bio	Cat#425581
RNAscope Probe *LAMP5*	ACD Bio	Cat#487691
RNAscope Probe *COL5A2*	ACD Bio	Cat#510911
RNAscope Probe *RORB*	ACD Bio	Cat#446061
RNAscope Probe *GAL*	ACD Bio	Cat#317631
RNAscope Probe *GABRG1*	ACD Bio	Cat#485931
RNAscope Probe *RPRM*	ACD Bio	Cat#565701
RNAscope Probe *PCP4*	ACD Bio	Cat#446111
RNAscope Probe *ROBO3*	ACD Bio	Cat#483191
RNAscope Probe *NR4A2*	ACD Bio	Cat#582621
RNAscope Probe *NTNG2*	ACD Bio	Cat#551651
RNAscope Probe *SNAP25*	ACD Bio	Cat#518851
RNAscope Probe *GABRA1*	ACD Bio	Cat#472141
RNAscope Probe *GRIN2B*	ACD Bio	Cat#485851
RNAscope Probe *SYT1*	ACD Bio	Cat#525791
RNAscope Probe *AFT4*	ACD Bio	Cat#405741
Critical Commercial Assays		
Chromium Single Cell 3’ v2 Reagent Kit	10x Genomics	PN-120237
RNAscope Multiplex Fluorescent Reagent Kit v2	ACD Bio	Cat#323120
RNAscope 2.5 HD Duplex Assay	ACD Bio	Cat#322430

REAGENT or RESOURCE	SOURCE	IDENTIFIER
Deposited Data		
Raw and processed data	This paper	GSE129308
Published dataset	Mathys et al., 2019	https://www.synapse.org/#!Synapse:syn18485175
Published dataset	Leng et al., 2021	https://cellxgene.cziscience.com/collections/180bff9c-c8a5-4539-b13b-ddbc00d643e6
Software and Algorithms		
Seurat	Seurat v2.4, v3 and v4	https://satijalab.org/seurat/
Fiji/ImageJ	Fiji v.2.3.1	RRID:SCR_002285
Adobe Illustrator CC	Adobe Systems	RRID:SCR_010279
SynGO	SynGO consortium	https://www.syngoportal.org/
g:Profiler	g:Profiler version Ensembl 97, Ensembl Genomes 44	https://biit.cs.ut.ee/gprofiler/gost
Cytoscape	Cytoscape v3.8.2	RRID:SCR_003032
Stereo Investigator	MBF Bioscience v.2018	RRID:SCR_002526
Cell Ranger	10x Genomics	RRID:SCR_017344